THESIS FOR THE DEGREE OF LICENTIATE OF ENGINEERING

# Electrical Characterization of Partial Discharge Resistant Enamel Insulation

ANH T. HOANG


High Voltage Engineering
Department of Materials and Manufacturing Technology
CHALMERS UNIVERSITY OF TECHNOLOGY
Gothenburg, Sweden 2014

**Electrical Characterization of Partial Discharge Resistant Enamel Insulation**

Anh T. Hoang



High Voltage Engineering
Department of Materials and Manufacturing Technology
Chalmers University of Technology
SE-41296 Gothenburg
Sweden
Telephone + 46 (0)31-772 1000

Chalmers Bibliotek, Reproservice
Gothenburg, Sweden 2014

**Electrical Characterization of Partial Discharge Resistant Enamel Insulation**

**Anh T. Hoang**

Department of Materials and Manufacturing Technology
Chalmers University of Technology

## Abstract

Adjustable speed drives for rotating machines have become increasingly popular as they provide possibilities of smooth and accurate process control as well as for energy savings. In such systems, due to the fact that the voltage applied at terminals of motor windings is no longer purely sinusoidal but characterized by a high content of harmonics, the appearing electrical and thermal stresses yield premature failures of the winding insulation, mainly because of an increased partial discharge (PD) activity. To tackle the problem effectively, PD-resistant enamels have been developed, by introducing various inorganic fillers into the base polymer of the wire insulation, that exhibit an increased resistance to PD activity. The effect seems, in most of the cases, to be strongly dependent on the dielectric properties of the filler used and the degree of interactions with the host materials.

In this respect, a recently developed enamel insulation, in which the top layer of the multilayered coating is filled with micro-particles of chromium (III) oxide ($Cr_2O_3$), has demonstrated exceptional properties. To elucidate the effect of material properties on the PD behavior, the presented in this thesis study concentrates on electrical characterizations of the new enamel insulation by measuring and analyzing its electric conductivity and complex dielectric permittivity and comparing these parameters with of the properties of enamel without the filler. In addition, the decay of surface potential induced by deposition on the enamel wire surfaces electric charges from a corona source is examined.

The performed analyses show that the addition of $Cr_2O_3$ filler results in a highly conductive and dispersive material, as compared to the base enamel. As a consequence, the top coating layer of the enamel wire insulation activates suppression of PD activity, while the insulating properties of the bulk material are kept unchanged. The presence of chromium oxide results in enhanced interfacial polarization and low frequency dispersion (hopping conduction) of the enamel. The material conductivity is increased because of enhancement of charge carrier mobility as well as a shift of the maximum of trap density distributions towards lower energy levels. The mechanism of the surface potential decay is analyzed by means of a model in which the combination of charge injection, dipolar polarization and intrinsic conduction appears to be the most important contributors to the observed surface charge dynamics.

**Key words:** enamel wire insulation, chromium oxide, dc conductivity, dielectric permittivity, charge injection, charge transport, dipolar polarization, partial discharge, twisted pair.

# Acknowledgments

First and foremost, I would like to express my deepest gratitude to my supervisor Assoc. Prof. Yuriy Serdyuk for his valuable guidance, consistent support, for always being ready to discuss new obtained results, and carefully revising all my manuscripts. From the bottom of my heart, I would like to thank my examiner and co-supervisor Prof. Stanislaw Gubanski for his guidance, kind support, motivation throughout the project, and critical comments on the experimental outcomes. I am grateful to the members of the reference group, Dr Göran Paulsson and Dr. Henrik Hillborg, for fruitful discussions as well as for providing material samples for this investigation.

The present work has been performed with the financial support from Chalmers Energy Initiative, which I gratefully acknowledge. The travel grant provided by the "Schneider Electric's fund in memorial of Erik Feuk" for participation in conferences is acknowledged.

I would like to take this opportunity to thank all the staff of the High Voltage Engineering group, of which I am proud to be a member. I really appreciate many helpful comments and advice they gave me in various discussions. I would like to acknowledge Dr. Sarath Kumara, a former PhD student of the group, for creating a great test setup for surface potential decay measurements. My thanks also go to Thomas Hammarström for collaboration in partial discharge measurements, to Dr. Yuesheng Zheng for discussions on the nonlinear fitting method, and to Xiangdong Xu for help in the contact-free measurements. Colleagues from division of Electric Power Engineering are thanked for creating a pleasant working environment.

I thank Dr. Tung T. Hoang and Dr. Tuan A. Le for their supports during my time at Chalmers. Thanks are also to all my Vietnamese friends in Gothenburg for creating enjoyable activities outside university and helping in numerous matters.

Last but most significant, my family is sincerely thanked for love, understanding, and moral supports. Their continuous encouragements are really valuable to me on every step of my life.

Anh T. Hoang
Gothenburg, Sweden
April 2014

# Table of contents

# 1 Introduction

## 1.1 The project

Adjustable speed drives have gained a widespread application due to a number of provided technical benefits. In particular, the use of fast switching power electronics allows for saving significant amount of energy. However, the applied voltages containing high frequency harmonics put winding insulation of electric motors at risk of failure. The continuous exposure of insulation systems to the distorted voltages increases the risk of enhanced partial discharge (PD) activity and space charge accumulation, thus causing accelerated aging and premature failure [1-3]. To deal with the problem, filtering techniques are sometimes employed for reducing the high frequency content, which are not always the most cost-effective option. Therefore, the use of PD-resistant enamel insulation is usually the first priority among all other measures. Such insulations are commonly created by introducing layered enamel structures and adding micro- or nano-particles of inorganic fillers into a base polymeric material [4, 5]. The doping degree is not to be necessarily high, an addition of nano-fillers at few wt% allows for significant lengthening the insulation life time [5].

A possibility of using chromium oxide $Cr_2O_3$ filler for improving the PD resistance of enamel insulations was noted in 1990s. Thus, an enamel insulation containing an unfilled base coating and micro-filled top coating has been created, showing a considerable increase in time to breakdown as compared to a conventional insulation [6]. The idea has been renewed recently by combining a nano-filled base coating with the $Cr_2O_3$-filled top coating [7]. Since the former also contributes to the material PD resistance, the synergy effect is anticipated for the newly developed enamel insulation. The performed accelerated aging tests at high temperatures revealed that the life time of such insulation is substantially increased as compared to both the conventional and the early developed enamel with filler in the top coating only [7]. This outstanding outcome requires a reasonable explanation, which in turn may aid the production technology of enameled wires.

In this work, instead of focusing on the aging tests as done in most of the investigations performed in this particular topic, fundamental electrical properties of the enamel insulation with and without chromium oxide filler are studied. Firstly, the effect of the filler on conduction and polarization mechanisms in the materials is analyzed utilizing experimental results on volume conductivity and dielectric permittivity obtained at different temperatures. Further, surface potential decay measurements are used for exploring the dynamics of charges on enameled wire surfaces as well as for deriving microscopic material properties. Finally, PD behavior of the materials is studied and correlated with the obtained dielectric properties.

To simplify insulation structure and to avoid effects of the nanofiller in material properties, on the present stage of the work, the experiments were conducted for enamel insulation with chromium oxide added only in the top coating, which is referred to as the filled enamel throughout the thesis. An enameled wire with conventional insulation has been used as a reference in the study. The enamel insulation with fillers in both layers is planned to be used later for PD measurements.

## 1.2 Outline of the thesis

The structure of the thesis is as follows.

Chapter 2 presents results of the measurements of volume electric conductivity and dielectric permittivity of the enamel insulations. At first, a brief overview on the dielectric properties of all phases in the filled enamel is provided. Further, the measured properties of the considered materials are presented in terms of their temperature and frequency dependences. Next, the dielectric permittivity obtained using a master curve derived for a frequency range wider than the experimental window is discussed. Contributions of dipolar polarization, low frequency dispersion, and dc conduction in the polarization relaxation process of the studied materials are examined. Finally, a model of the filled enamel created for verifying the measured results and for analyzing changes in local electric field distributions is presented.

Chapter 3 focuses on the potential/charge decay process on enamel insulation surfaces. The chapter starts with an overview of decay mechanisms and theories allowing for deriving microscopic properties of insulating materials from the measured decay characteristics. Results of the experiments (distributions and decay of surface potentials and charges) conducted on winding samples pre-charged by corona from nearby sharp electrodes are presented. Based on these, possible surface charge decay mechanisms are discussed and contributions of several processes, e.g. charge injection into enamel, trapping and de-trapping, dipolar polarization, are analyzed. Finally, characteristics of the studied materials deduced from the experimental data, such as trap density distributions and charge carriers mobilities, are discussed.

In chapter 4, preliminary results of partial discharge characteristics are presented for enamel insulations exposed to PWM voltages at three filtering options. PD inception and extinction levels as well as PD amplitudes and numbers per cycle are compared for the filled and the conventional enamels. The influence of the filler on the obtained PD characteristics is discussed.

The conclusions from the work performed are summarized in chapter 5 and suggestions for future work are provided in chapter 6.

## 1.3 List of publications

1. Anh T. Hoang, Yuriy V. Serdyuk, and Stanislaw M. Gubanski, "Electrical Characterization of a New Enamel Insulation," accepted for publication in the *IEEE Transactions on Dielectric Electrical Insulation*, 2014.
2. Anh T. Hoang, Thomas J. Å. Hammarström, Tord Bengtsson, Yuriy V. Serdyuk, and Stanislaw M. Gubanski, "Partial Discharge Behavior of a Newly Developed Enamel Insulation at Various Voltage Rise Times," 7th International Symposium on Electrical Insulating Materials (ISEIM 2014), June 1-5, 2014, Niigata City, Japan, accepted.
3. Anh T. Hoang, Yuriy V. Serdyuk, and Stanislaw M. Gubanski, "Charge Decay on Enamel Wire Surface," International Conference on High Voltage Engineering and Application (ICHVE 2014), September 8-11, 2014, Poznan, Poland, accepted.

# 2 Dielectric properties of enamel insulation

## 2.1 Literature review

This section provides a summary on dielectric properties of components in the filled enamel insulation.

### 2.1.1 Properties of enamels

Enamel wire insulation usually has a multilayered structure that consists of at least of two layers, a base coat and a top coat. The materials used for creating these layers are usually polyester-imide (PEI) for the former and polyamide-imide (PAI) for the latter. They are both high temperature materials with stable thermal properties. Chemical structure of the repeating unit of PAI is shown in Figure 2.1. For both the materials, the glass transition temperature ($T_g$) is approximately 270 °C [8, 9].

The dielectric permittivity of PAI has been reported in [8] for a wide range of temperature (from –100 °C to 400 °C) and frequency ($10^{-1}$-$10^{6}$ Hz). At temperatures below 200 °C, the real part of complex permittivity varies from 4 to 4.5, depending on the frequency of the applied voltage. For the temperature close to $T_g$, the real part of complex permittivity increases rapidly with reducing frequency.

The dc conductivity of PAI has been derived in [8] from the ac conductivity measured at the frequency of 0.1 Hz. At 250 °C, the obtained dc conductivity is ~$10^{-11}$ S/m. For temperatures above $T_g$, dc conductivity of the material follows the nonlinear temperature behavior.

It should be noted that not much information is available about the thermal and dielectric properties of PEI. The measurements performed in a frequency range of ~$10^{1}$-$10^{5}$ Hz [9] showed that the real part of the complex permittivity increases monotonously from 4.2 to 5 with decreasing frequency and the loss factor (tan$\delta$) is ~$10^{-2}$ and is characterized by two loss peaks at ~$10^{2}$ Hz and $10^{5}$ Hz.

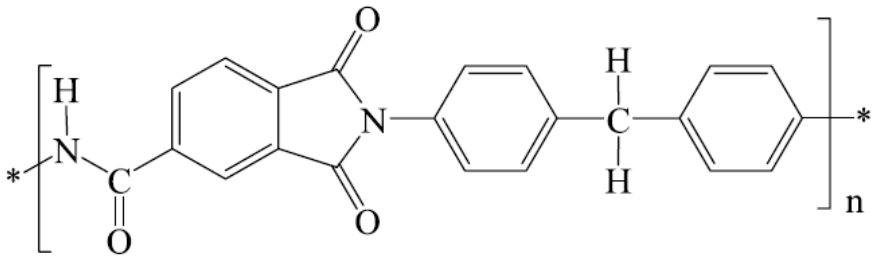


*Figure 2.1. Chemical structure of the repeating unit of PAI.*

### 2.1.2 Properties of chromium oxide

Chromium (III) oxide $Cr_2O_3$ is widely used as a pigment in the paint industry due to its characteristic green color. Being added to enamel insulation it provides the material with the same hue.

Volume electrical conductivity of chromium oxide has been reported in several works, for example [10-13]. Crawford and Vest [10] have described two conduction mechanisms of chromium oxide crystals, namely defect-controlled and intrinsic conduction. The defect-controlled mechanism occurs below a characteristic temperature (~1000 K), and is affected by external conditions. It is caused by defects in material crystals that generate charge carriers by reaction with oxygen. Consequently, the electrical conductivity strongly depends on the partial pressure of oxygen. On the other hand, the intrinsic mechanism is observed above the characteristic temperature and it is unaffected by external conditions. In such a case, the conduction is created by the charge transfer between ions of molecule $Cr_2O_3$ through the formation of either an electron-hole pair or a hole. The experimental results show that in the temperature range 600-1400 °C, the electrical conductivity is as high as $10^{-2}$-10 S/m for chromium oxide crystals in oxygen at pressures of $10^{-2}$ to 1 atm [10]. Further, the volume conductivity of material in the form of thin films strongly depends on temperature and sample thickness [11]. The conductivity increases significantly with increasing temperature, whereas it decreases dramatically with increasing material thickness. For example, at 25 °C the electrical conductivity of a chromium oxide film with thickness of 125 nm is of ~1 S/m and it is $10^{-6}$ S/m for the bulk of $Cr_2O_3$ in mm range. Gas medium and gas pressure also affect the measured volume conductivity of chromium oxide. For instance, it is increased considerably in oxygen environment as compared with the case of vacuum.

The conductivity measurements reported in [12] have been performed at high temperatures (200-500 °C) for chromium oxide powder used as a catalyst. Experiments have been conducted in different gas media and showed that the volume conductivity varied in a range $10^{-9}$-$10^{-7}$ S/m for vacuum, $10^{-8}$-$10^{-6}$ S/m for hydrogen environment, and it was significantly higher ($10^{-5}$-$10^{-2}$ S/m) for oxygen medium. Besides, the values $10^{-1}$-10 S/m were recorded for porous specimens immersed in oxygen in temperatures 550-1300 °C [13]. The variations in the magnitudes of the volume conductivity of chromium oxide in vacuum, hydrogen and oxygen have been explained by differences in conduction mechanisms and types of charge carriers. Thus, positive carriers (holes) were suggested to be dominant in the material exposed to oxygen whereas negative charge carriers (electrons) were assumed to be prevalent in chromium oxide in hydrogen medium.

The relative permittivity (the real part of the complex permittivity) of chromium oxide has been measured in [14] using a single crystal of 6 mm in diameter and 0.5 mm in thickness at room temperature (25.5 °C) and frequency of 1 kHz and 2 MHz. Since the material has the corundum structure (hexagonal system) [10], its relative permittivity is anisotropic and it was determined for two directions, namely directions parallel to *a* axis and parallel to *c* axis. The relative permittivity value of 13.3 has been recorded at 1 kHz and 13.0 at 2 MHz for the first direction, whereas it was 11.9 at 1 kHz and 11.8 at 2 MHz for the second direction. Furthermore, the relative permittivity was found to be weakly dependent on temperature and the magnitude of the temperature factor was found to be ~$10^{-3}$ $K^{-1}$ for the range 25-52 °C. In summary, the average value of the relative permittivity of chromium oxide can be taken as approximately 12-13. An increase in the relative permittivity of filled enamel is therefore anticipated due to the presence of highly dispersive chromium oxide in the conventional polyamide-imide insulation.

## 2.2 Measurements with flat samples

The measurements were initially carried out for flat samples of polyamide-imide (PAI) resin and resulted in a limited amount of reliable data. The reasons for that seem to be of generic character for enamel materials and, therefore, are discussed here together with the main results obtained.

Flat materials samples were created by depositing a thin insulation layer on top of the substrate that was a copper plate of 1 mm in thickness and having square shape with a side of 100 mm. The insulations used were PAI resin without any fillers and PAI resin containing chromium oxide filler at 14.3 wt% (equivalent to 4.3 vol%). The insulation thickness was 38 and 19 μm for the PAI and $Cr_2O_3$-filled PAI layers, respectively. Note that an insulation layer with an evenly distributed thickness can be hardly prepared from this type of material and this non-uniformity is considered as the main reason for the limited applicability of flat samples.

The volume conductivity measurements were conducted in accordance with the IEC standard 60093 [15] in a three-electrode arrangement (Figure 2.2). In the test cell, the metallic electrode was covered by a layer of soft semiconducting resin for assuring a good contact with the sample surface. Keithley Electrometer 6517A was utilized as a test voltage source and for measuring the current through the material. During the measurements, it was observed that a stable steady state current (true conduction current) could be registered after quite long time after voltage application when the polarization current ceased. The volume conductivities obtained at time $4\times10^4$ s are presented in Table 2.1 together with the electric field applied to the material. One may notice the increase in the conductivity due to the addition of chromium oxide, as expected. However, it was also noticed that once the applied electric field was enhanced, the shape of the polarization current changed drastically. Thus, for the $Cr_2O_3$-filled PAI resin, the time-dependent polarization current was not reducing gradually as expected, but instead, several peaks were observed in the current trace. An analysis showed that these might not be attributed to the polarization process in the material and appeared, most probably, due to the imperfection of the material samples, i.e. their uneven thickness. Hence, the measurements of volume conductivities with flat samples were found to be unreliable and the values shown in the table should be considered as indications providing orders of magnitudes only.

The measurements of complex permittivities were conducted by means of the Insulation Diagnostic System IDAX 300, which is equipped with an internal ac voltage source and measures the response current and phase shift, thereafter used for calculation of dielectric permittivity. To avoid the problem mentioned above, a contact-free technique [16] has been employed for measuring material permittivity. The idea of the method is to place the sample on the bottom electrode, while having no contact with the top electrode. The object under measurement can be represented as a series connection of two capacitors (the sample capacitor $C_{sample}$ and the capacitor $C_{air}$ of the air gap between the sample and the top electrode). Consequently, the sample capacitance can be calculated by using the measured result and geometric parameters of the arrangement. The method in general allows for improving the accuracy in dielectric measurements in such cases when samples are susceptible to deformation due to being pressed between two electrodes or good contact between specimens and electrodes cannot be achieved. Despite of these possibilities, a drawback of the method has become evident during the measurements. It is related to the fact that the samples used in the present study provided the material thickness in μm range, which is in one order of magnitude smaller than the air gap (0.3-0.4 mm), resulting in the relationship $C_{sample} >> C_{air}$. The total capacitance of the two capacitors connected in series is

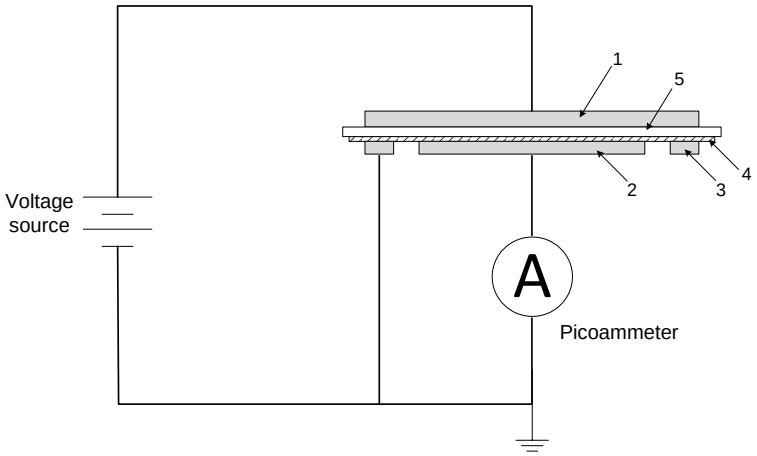


*Figure 2.2. Circuit for measuring volume conductivity of flat sample: 1 – voltage electrode, 2 – measuring electrode, 3 – guard ring, 4 – insulation, 5 – copper plate.*

*Table 2.1. Volume conductivity of PAI resin and that filled with $Cr_2O_3$*

| Material | Electric field, V/m | Volume conductivity, S/m |
|---|---|---|
| PAI | $1.05\times10^{6}$ | $3.9\times10^{-15}$ |
| $Cr_2O_3$-filled PAI | $0.53\times10^{6}$ | $7.8\times10^{-15}$ |

therefore mainly determined by the air capacitor $C_{air}$, leading to inaccuracy in calculating sample capacitance. In reality, the experiment provided unreasonable results (the real part of relative permittivity was always close to 1), which is obviously dissimilar to the values reported in [8]. As it is noted in [16], the accuracy of the contact-free measurement depends on the filling ratio that is the ratio of the sample thickness to the thickness of the total air gap between two electrodes. An optimum filling ratio should be larger than 0.7. In the present study, however, the filling ratio was less than 0.1 that contributed to the large measuring error. The measurement could be improved by reducing the air gap between the sample surface and the top electrode to a value lower than 30 μm. However, this will increase the error in thickness measurement, which in turn also negatively affects the measuring accuracy.

In summary, several problems arising in the conductivity and permittivity measurements for flat samples of unfilled and filled PAI layers limited their applicability and reduced the accuracy of the results obtained. As the second alternative, the dielectric measurements were subsequently performed for the wire samples.

## 2.3 Experiments with enameled wire samples

Two types of enameled wires, one having a conventional and the other a filled insulation, were used in experiments. Their cross sections are illustrated in Figure 2.3. The conventional enamel insulation had three layers (a PEI base coat, a PAI over coat, and a modified aromatic polyamide (PA) bonding coat), whereas the filled enamel had two layers (a PEI base coat and a PAI top coat). The top coat of the latter was filled by 26 wt% (equivalent to 8.7 vol%) of chromium oxide micro-particles, whose size varied between 0.2 and 2 μm (the average size

was 0.74 μm). The diameter of the wires in both cases was 1.18 mm, whereas the insulation thickness was respectively 50 and 40 μm for the conventional and the filled enamel layers.

The volume conductivity of the enamel insulations was measured by the standard method using a Keithley Electrometer 6517A. A three-electrode system was designed, in which the high voltage was supplied to the wire conductor, whereas the measuring and the guard electrodes were made of conductive copper tapes attached to the external enamel layer (Figure 2.4). The measuring and the guard electrodes were 4 cm and 1 cm in length, respectively. The electrode arrangement was placed in a metallic grounded box, which also allowed for controlling temperature and humidity during the measurements. In particular, tests were performed at room temperature (22-24 °C), and at 40, 60 and 80 °C, which were achieved by using a heater and a thermostat. On the other hand, the relative humidity was maintained in the range of 30-40% by a saturated salt solution. The applied voltage was set at 100 V, corresponding to the electric stress of approximately $10^6$ V/m. The resulting volume conductivity $\sigma$ was determined as

$$\sigma = \frac{I \cdot d}{U \cdot A} \tag{2.1}$$

where $I$ is the measured current, $U$ is the applied voltage, $A$ is the area of the measuring electrode and $d$ is the insulation thickness.

The dielectric spectroscopy measurements were carried out in the frequency range from 1 mHz to 1 kHz by means of an Insulation Diagnostic System IDAX 300. The shielding box was also employed here for reducing the influence of parasitic capacitances between the sample and the ground potential on the measured capacitance. In this case, the external electrodes on wire samples were created by depositing thin layers of silver paint for eliminating the influence of series capacitances on the determination of permittivity and the

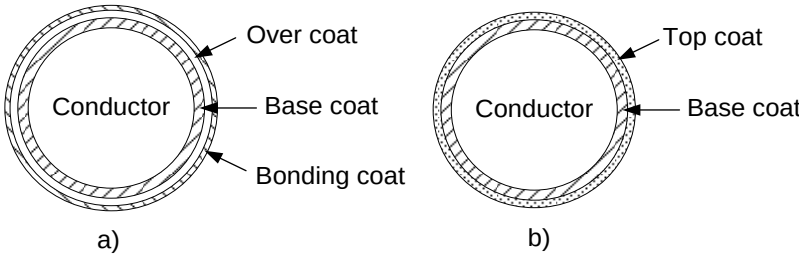


*Figure 2.3. Cross sections of conventional (a) and filled (b) enameled wires.*

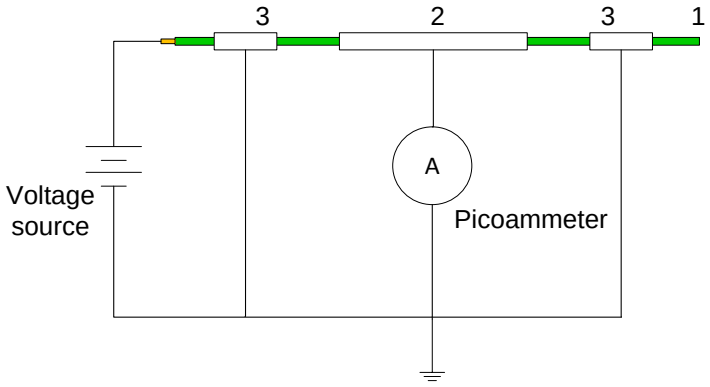


*Figure 2.4. Circuit for measuring volume conductivity of enamel coating: 1 – enameled wire, 2 – measuring electrode, 3 – guard electrode.*

lossy glue layer in the conductive tape. Temperature and humidity were maintained during the measurements in a similar range as for the conductivity measurements. Thermal equilibrium inside the shielding box was achieved by keeping it in an oven for ~2 h. Thereafter the experiments were carried out by applying the ac voltage of 100 Vrms. The complex permittivity of a sample was obtained by dividing the measured complex capacitance by the geometric capacitance of the samples.

## 2.4 Measurements with $Cr_2O_3$ powder

A specialized test cell (Figure 2.5), consisting of two concentric stainless steel cylinders and a guard ring, was additionally used for measuring the dielectric properties of chromium oxide powder. The inner cylinder acted as the high voltage electrode, while the measuring and the guard electrodes were located in the bottom of the outer cylinder. The diameters of the energized and the measuring electrodes were 30 mm and 13.1 mm, respectively. The investigated powder was first dried at 120 °C for 24 h, and then poured into the cell to form after pressing a thin layer (~1 mm thick) between the voltage and the measuring electrodes. Depending on the type of measurement (dc conductivity or dielectric permittivity) voltages up to 4 V were used.

## 2.5 Experimental results

This section provides the comparison of electrical conductivity and complex permittivity between the filled and the conventional enamels. Dielectric properties of chromium oxide powder are also analyzed. Three consecutive measurements were carried out at each of the test temperatures and a good repeatability of the results was achieved.

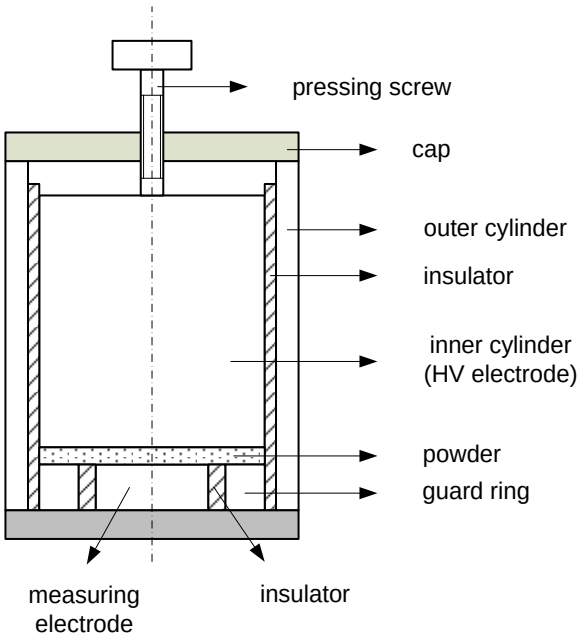


*Figure 2.5. Schematic diagram of the test cell for measuring dielectric properties of powder.*

### 2.5.1 Electrical conductivity

Typical measured volume currents for both types of the enamels are shown in Figure 2.6. For the sake of clarity, only the results obtained at the lowest (22 °C) and the highest temperatures (80 °C) are presented. One may observe that the measured currents decayed with time. They were practically independent of the material type and temperature within the first 50 s. This could be explained by the dominance of a capacitive current during the initial stage, governed by similar capacitances of the two types of samples. After ~1000 s however, the measured currents were significantly different and the temperature effect was pronounced. Thus, the current increased by one order of magnitude as the temperature rose from 22 °C to 80 °C for both types of the insulation. To find conductivity values, the conductive current component has to be determined and it can only be achieved after a long measuring time when the capacitive component of the current ceases. As can be seen in this particular case, the current decayed even after $10^5$ s (~28 h) and its purely conductive level was hardly achievable. Therefore, the measurements were stopped after $10^5$ s for practical reasons and the conductivities were calculated from the corresponding current magnitudes.

As seen in Figure 2.7, the obtained volume conductivities for both the enamel insulations are in general lower than the values obtained with flat samples (Table 2.1) and obey Arrhenius relation:

$$\sigma(T) = \sigma_0 \exp\left(-\frac{W_c}{kT}\right) \tag{2.2}$$

where $\sigma_0$ is a constant parameter, $W_c$ is the activation energy for the conduction, $k$ is the Boltzmann constant, $T$ is the temperature. One may notice that the volume conductivity of the two materials is extremely low, but still higher for the filled enamel than for the conventional one. The calculated activation energies are 0.33 eV and 0.46 eV for the conventional and the filled enamels, respectively.

The conventional enamel coating used in this study can be considered as a series connection of three resistors corresponding to three layers in its structure. The measured volume conductivity of the conventional enamel is around two orders of magnitude lower than that of PAI obtained in section 2.2. For the other two materials, the parameter is unknown, but one can expect PEI to be the most resistive, while modified aromatic PA as the most conductive among the three constituents of the considered enamel. Thus, the resistance of three resistors in series will be determined by that of the PEI base coat. In other words, the volume conductivity of PEI should be close to that of the conventional enamel (~$10^{-17}$ S/m), while PAI and aromatic PA are characterized by a volume conductivity $\sigma \geq 10^{-15}$ S/m. The volume conductivity of chromium oxide powder measured at room temperature and at electric fields ~$10^3$ V/m is shown in Table 2.2. Note that it is eight orders higher than that of the enamel insulations. However, its impact on the conductivity of the filled enamel is limited as exhibited in earlier studies. The reason is that the filler modifies the property of the PAI top layer only, whereas the resistive PEI base coat remains unchanged.

The electrical conductivity of chromium oxide has been reported in several studies performed for the material in different physical states such as crystal grown from powder [10], thin film [11], powder [12] and porous specimens [13]. It is commonly emphasized that the exposure of the material to oxygen increases the average valency of surface chromium ions, giving rise to the density of positive charges. The accumulated charges might be reduced at room

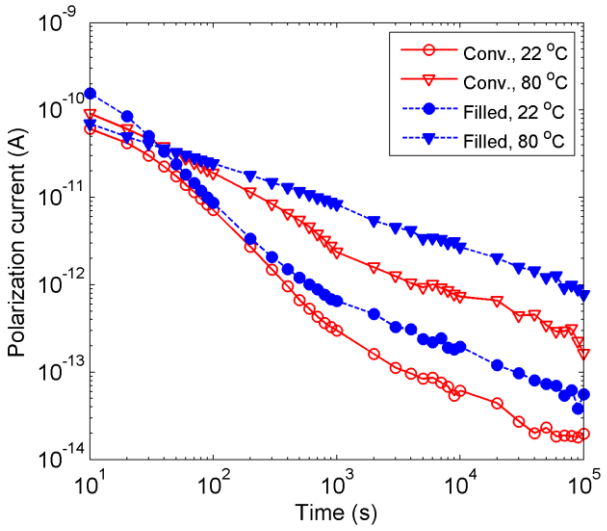


*Figure 2.6. Time variations of polarization currents of conventional and filled enamels.*

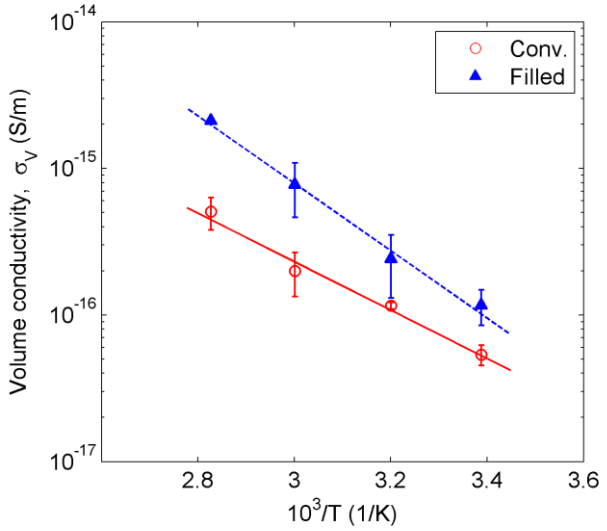


*Figure 2.7. Temperature dependence of volume conductivity of conventional and filled enamels. The conductivity has been calculated based on current value at $10^5$ s after test voltage application.*

*Table 2.2. Volume conductivity of chromium oxide powder at room temperature*

| E, V/m | $0.71\times10^{3}$ | $1.43\times10^{3}$ | $2.86\times10^{3}$ |
|---|---|---|---|
| σ, S/m | $0.50\times10^{-7}$ | $1.00\times10^{-7}$ | $1.24\times10^{-7}$ |

temperature, yet they may still contribute to the conduction mechanism. As it is shown in [12], the conductivity of chromium oxide follows the Arrhenius dependence in the temperature range from 140 to 450 °C. Thus, an extrapolation using these data can be performed to obtain the electrical conductivity of chromium oxide at room temperature. This procedure provided a value $7.2\times10^{-8}$ S/m that is in agreement with the measured results. This suggests a presence of space charges in the material in our experiments.

## 2.5.2 Complex permittivity

### 2.5.2.1 Complex permittivity of enamels

Real and imaginary parts of the complex permittivity measured at various temperatures are shown in Figures 2.8 and 2.9 for the conventional and filled enamels, respectively. As it is seen, at frequencies below 10 Hz, the imaginary part (dielectric loss) increased more rapidly with reducing frequency, whereas the real part showed a gradual rise in the whole frequency range. On the other hand, temperature affected those parameters differently: while the temperature rise reduced the real part at frequencies above 1 Hz, it considerably increased the imaginary part. It should be noted that coefficients of thermal expansion are low for both polymeric materials (less than $4\times 10^{-5}$ $K^{-1}$ [17, 18]) and for copper conductor (~$1.7\times 10^{-5}$ $K^{-1}$ [19]), thus causing the thermal expansion less than 0.3% for the enamel layers and the wire conductor. Apparently, this could not account for the decrement of the real part of the complex permittivity, which was as high as 10% when the temperature increased from 24 to 100 °C. Localized maxima were observed in the loss curves of conventional enamel (Figure 2.8b). They shifted towards higher frequencies and became more considerable as temperature rose. However, such localized peaks were not observed in the loss curves for filled enamel (Figure 2.9b). In general, the magnitudes of the real and imaginary parts of the complex permittivity were higher for the filled enamel than for the conventional counterpart that can be attributed to the influence of highly dispersive and conductive chromium oxide filler.

### 2.5.2.2 Complex permittivity of chromium oxide powder

The real and imaginary parts of the complex permittivity of chromium oxide powder exhibited a rapid grow with reducing frequency (Figure 2.10). The slopes of the curves for both parameters are around –0.9 indicating the dominance of the low frequency dispersion process, which can be attributed to charge accumulation in the volume and its transport due to hopping between traps [20]. Aside from the low frequency dispersion, the temperature dependence of the complex permittivity of chromium oxide is noteworthy. Both the real and imaginary parts initially rose with temperature, reaching their maxima at around 60 °C, and then decreased again as the temperature continued growing up. This indicates the presence of a relaxation process with a loss peak at this temperature.

The relative permittivity of chromium oxide has also been measured in [14] for a single crystal of 6 mm in diameter and 0.5 mm in thickness. The experiment conducted at room temperature at frequencies of 1 kHz and 2 MHz yielded a practically constant value of 12-13. In spite of the fact that the test object and the electrical stress utilized in our measurements differ from those employed in [14], our measured result at frequency of 1 kHz is in line with that received in [14].

Although chromium oxide is relatively highly conductive and dispersive, its addition into polymeric insulation does not enhance corresponding properties of the filled enamel drastically, proving that the percolation level is not reached. In particular, for statistically distributed spheres in three dimensions the theoretical percolation threshold would be ~15 vol% [21], which is larger than the percentage of the additive in the top coat of the filled enamel (8.7 vol%). Thus, molecular chains and amorphous state of PAI isolate micro-particles of chromium oxide one from another; thereby hindering an easy transfer of the space charges. In addition, chromium oxide fillers only modify dielectric properties of the top coat in the filled enamel. Consequently, low frequency dispersion should be detected in the characteristics of filled enamel, but it would not be as strong as that presented in the behavior of chromium oxide powder.

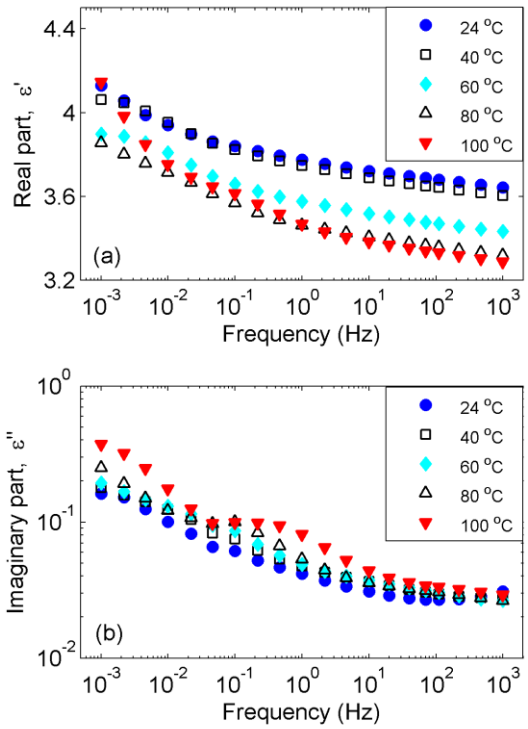


*Figure 2.8. Real (a) and imaginary (b) parts of the complex permittivity of conventional enamel at different temperatures.*

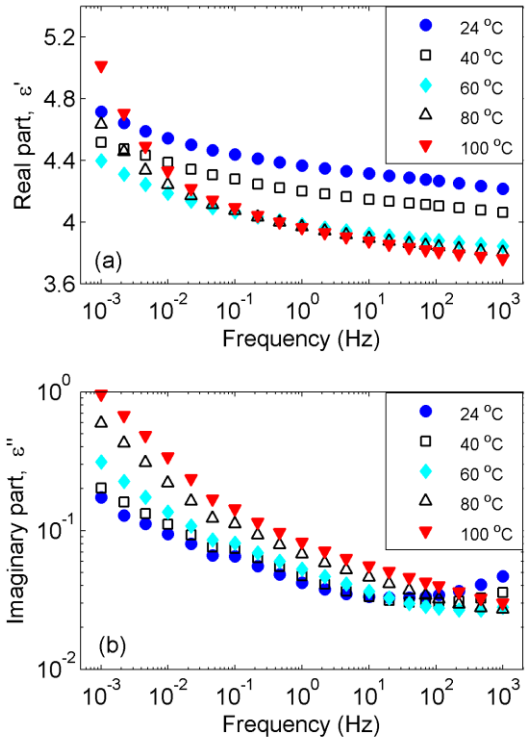


*Figure 2.9. Real (a) and imaginary (b) parts of the complex permittivity of filled enamel at different temperatures.*

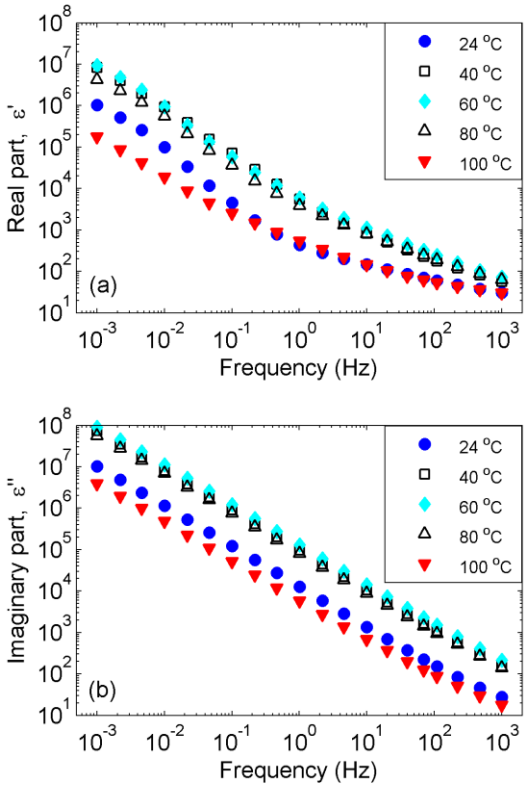


*Figure 2.10. Real (a) and imaginary (b) parts of the complex permittivity of chromium oxide powder at different temperatures. Note that measured results at 40, 60 and 80 °C are close.*

## 2.6 Analyzing polarization processes in enamel insulations

### 2.6.1 Master curve of dielectric response

One can observe that for each of the materials, the shapes of the frequency-dependent complex permittivities resemble one another when the temperature increased. This is due to the fact that material properties do not change significantly in the studied temperature range which was far below the glass transition temperatures of base polymeric materials (which is ~270 °C [8, 9]). Hence, the data can be normalized for obtaining a master curve representation [22]. In terms of complex dielectric susceptibility $\chi^*$, its frequency dependence at temperature $T_1$ can be achieved by shifting the corresponding characteristic at temperature $T_2$ laterally and vertically:

$$\chi^*(\omega:T_1) = k_a \cdot \chi^*(A\omega:T_2). \tag{2.3}$$

Here, $\chi^*(\omega) = \varepsilon^*(\omega) - \varepsilon_{hf}$, $\varepsilon^*(\omega)$ is the complex dielectric permittivity as a function of the angular frequency $\omega$, $\varepsilon_{hf}$ is the dielectric permittivity at high frequencies, $A$ is the factor of the lateral translation corresponding to the frequency shift, $k_a$ is the factor of the vertical translation (the amplitude shift). Theoretically, the real part of the complex susceptibility at a particular frequency can be estimated by using the Kramers–Kronig relation. The obtained value is then subtracted from the real part of the measured complex permittivity at the same frequency for gaining the permittivity at high frequencies. However, the data measured in the

present study (performed within six decades of frequency) do not allow for calculating $\varepsilon_{hf}$ by this procedure. Therefore, the master curve was achieved for the complex permittivity rather than for the complex susceptibility. For this, the susceptibility (2.3) was split into the real and imaginary parts:

$$\chi'(\omega:T_1) = k_a \cdot \chi'(A\omega:T_2) \tag{2.4}$$

$$\chi''(\omega:T_1) = k_a \cdot \chi''(A\omega:T_2) \tag{2.5}$$

which can be further represented as

$$\varepsilon'(\omega:T_1) - \varepsilon_{hf1} = k_a \cdot \left[ \varepsilon'(A\omega:T_2) - \varepsilon_{hf2} \right] \tag{2.6}$$

$$\varepsilon''(\omega:T_1) = k_a \cdot \varepsilon''(A\omega:T_2). \tag{2.7}$$

Here, $\varepsilon_{hf1}$ and $\varepsilon_{hf2}$ are the high frequency permittivities at temperatures $T_1$ and $T_2$, respectively. Equation (2.6) can be rewritten:

$$\varepsilon'(\omega:T_1) = k_a \cdot \varepsilon'(A\omega:T_2) + \left[ \varepsilon_{hf1} - k_a \cdot \varepsilon_{hf2} \right]. \tag{2.8}$$

The normalization procedure was initially conducted for the loss part. It should be noted that the contribution of dc loss $\sigma_{dc}/\omega\varepsilon_0$ ($\varepsilon_0$ is the vacuum permittivity) in the measured dielectric loss $\varepsilon''(\omega)$ is insignificant (less than 6%). Therefore, the subtraction of dc loss from the measured total loss before normalization, as described in [20], can be ignored as this introduces just a minor error. The same translation factors used for normalizing the loss were subsequently utilized for normalizing the real part of the complex permittivity. This resulted in a small discrepancy between the curves of the relative permittivity at different temperatures, which is due to the second component in the right hand side of (2.8). Since this component is independent on frequency, a vertical shift is to be introduced to compensate the influence of the permittivities at high frequencies.

The obtained master curves for the reference temperature of 24 °C are shown in Figure 2.11. The frequency shift $A$ of the response can be described as a function of temperature [23]:

$$A(T) = A_0 \exp\left( -\frac{W_p}{kT} \right) \tag{2.9}$$

where $A_0$ is a constant parameter, $W_p$ is the activation energy for polarization, which is 0.60 and 0.63 eV for the conventional and filled enamels, respectively.

The contribution of different processes (dielectric relaxation, dc conduction, low frequency dispersion) to the dielectric properties of the materials can be identified by analyzing the curves. One can observe that for both materials, the studied frequency range can be divided into three intervals limited by characteristic frequencies, at which the behaviors of the curves change. The first characteristic frequencies ($f_1$) are ~$10^{-4}$ Hz and ~$3\times10^{-4}$ Hz for the conventional and filled enamels, respectively, while the second ones ($f_2$) are ~70 Hz for both materials. Three intervals are marked in Figure 2.11 by vertical lines. In the first interval, the slopes of the loss curves are respectively –0.34 and –0.47 for the conventional and the filled enamels, whereas the slopes of the relative permittivity curve are less than –0.08. Hence, as

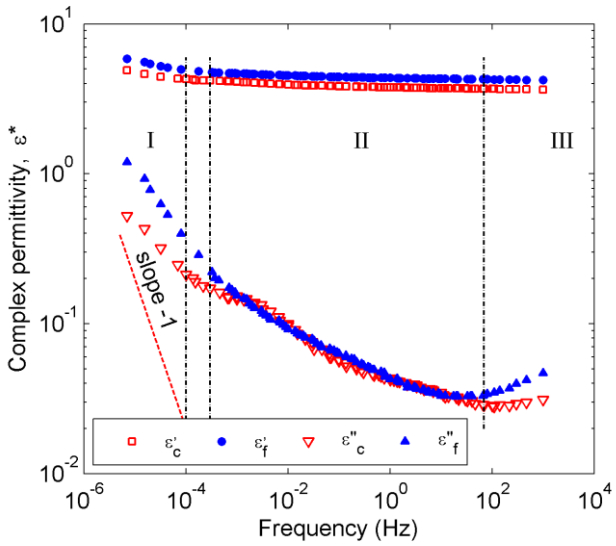


*Figure 2.11. Master curves of complex permittivity for both enamels at the reference temperature of 24 °C. The indexes c and f represent conventional and filled enamels, respectively. A line with slope of –1 is introduced for comparison with the slopes of the dielectric loss curves at low frequencies.*

the slopes of the loss curves are far from –1, dc conduction is not the prevalent process in the considered frequency interval [20]. In addition, as the slopes are different for the real and the imaginary parts of the complex permittivities, low frequency dispersion is also not the sole process in both studied materials [20]. This suggests that a dielectric relaxation process with a loss peak at some frequency below $f_1$ should be present in both enamels, which is superimposed in the above-mentioned processes. In the second interval, a localized loss peak apparent at frequency of ~$10^{-3}$ Hz in the characteristics of the conventional enamel may be attributed to the existence of a relaxation process. At the same time, the loss curve of the filled enamel shows a power-law behavior (with the slope –0.2) without a loss peak that could be owing to the change in the properties of enamel insulation brought about by chromium oxide fillers. In the third interval, an increase in the imaginary part is observed for both materials. This possibly implies the existence of yet another relaxation process with a loss peak at frequencies outside our experimental window. A detailed analysis on the origin as well as the contributions of different relaxation processes is discussed in the following section.

### 2.6.2 Modeling dielectric susceptibility of enamels

The dielectric susceptibility can be modeled by considering the contributions of dielectric relaxation, dc conduction and low frequency dispersion [23]. By assuming that three polarization relaxation processes take place in the studied materials, the complex dielectric susceptibility as a function of the angular frequency can be expressed as

$$\chi^*(\omega) = \sum_{j=1}^{3} \frac{\chi_{sj}}{\left(1+(i\omega\tau_j)^{\alpha_j}\right)^{\beta_j}} + \frac{\sigma_{dc}}{i\varepsilon_0\omega} + \frac{\varsigma}{\varepsilon_0 (i\omega)^{\gamma}}. \qquad (2.10)$$

Here, the dielectric relaxation (the first term) is described by the Havriliak–Negami expression, the index $j$ represents relaxation processes ($j$ = 1, 2, 3), $\chi_{sj}$ is the dielectric susceptibility at $\omega$ = 0 Hz, $\tau_j$ is the relaxation time, $\sigma_{dc}$ is the dc conductivity, $\alpha_j$, $\beta_j$, $\varsigma$, $\gamma$ are constant parameters, $0 < \alpha_j, \beta_j, \gamma \leq 1$. The dc conductivity obtained in section 2.5.1 was used

as an input parameter of the model. The obtained master curves were fitted using a nonlinear least-square method, which is achieved by minimizing the relative error $\theta$ between the experimental (index *exp*) and modeled (*m*) values of the real and imaginary parts of the complex susceptibilities:

$$\theta = \sum \left[ \left( \frac{\chi'_{\exp} - \chi'_m}{\chi'_{\exp}} \right)^2 + \left( \frac{\chi''_{\exp} - \chi''_m}{\chi''_{\exp}} \right)^2 \right]. \tag{2.11}$$

The results of the fitting are shown in Figures 2.12 and 2.13 for the conventional and filled enamels. As seen, the low frequency dispersion (hopping conduction) and the third relaxation process appear to be the main contributors to the real part of the dielectric susceptibility for both materials at low and high frequencies, respectively. On the other hand, three polarization relaxation processes and low frequency dispersion contribute mostly to the imaginary part of the dielectric susceptibility.

The behavior of the first relaxation process is similar in both enamels, yielding peak frequencies ~$10^{-5}$ Hz that allows for suggesting their identical origin. By considering the multilayered structures of the two insulation systems (Figure 2.3), one may suggest that Maxwell–Wagner–Sillars (MWS) polarization between the PAI and the PEI layers is the mechanism most likely acting in the materials. The loss peak frequencies of the interfacial polarization can be calculated by using dielectric properties of two polymers reported in [8, 9] as well as electrical conductivity measured in this study. The calculated results are ~$10^{-5}$ Hz, which are close to the values gained by the fitting, approving our assumption.

The second relaxation process is obviously different in the two enamels. The relaxation process arising in the conventional enamel is characterized by a broader response ($\alpha$ = 0.81, $\beta$ = 1) than the Debye relaxation with the loss peak frequency of $2 \times 10^{-3}$ Hz. It could be associated with the interfacial polarization between the PAI over coat and the aromatic PA bonding coat. Note however, that available data on the electrical conductivity of aromatic PA, PAI, PEI used in enamel insulation are limited and it is assumed that aromatic PA is more conductive than PAI and PEI. This may lead to a shift in the loss peak due to MWS polarization between PAI and PA layers to higher frequencies as compared to that of the MWS polarization between PAI and PEI layers. In the filled enamel, the second relaxation process ($\alpha$ = 0.30, $\beta$ = 1) is much broader than that corresponding to Debye relaxation, which yields the dielectric response without a localized peak. It could be due to the introduction of chromium oxide fillers into the PAI matrix. As their dielectric properties are clearly distinct, charges accumulate in their interfacial regions resulting in a MWS polarization. The highly conductive property of the additives, as shown in the section 2.5.1, leads to a higher frequency of the loss peak. It should be noticed that the accumulated charges may be trapped in localized traps inside the insulation and transferred by hopping between them, thus giving rise to the hopping conduction of the filled enamel [20]. Accordingly, the hopping conduction is the strongest component at frequencies between $10^{-5}$ and $10^{-2}$ Hz for the filled enamel, whereas the interfacial polarization between PAI and PEI layers is the main contribution to the dielectric loss at frequencies between $10^{-5}$ and $10^{-4}$ Hz for the conventional enamel. Besides, as the interfaces in the investigated systems are shortly apart, the interaction of charges accumulated due to MWS polarizations affects both of the relaxation processes.

Further, the third relaxation process in both materials dominates at high frequencies and provides the loss peak at frequency ~$10^{5}$ Hz, which is possibly owing to the dipolar relaxation

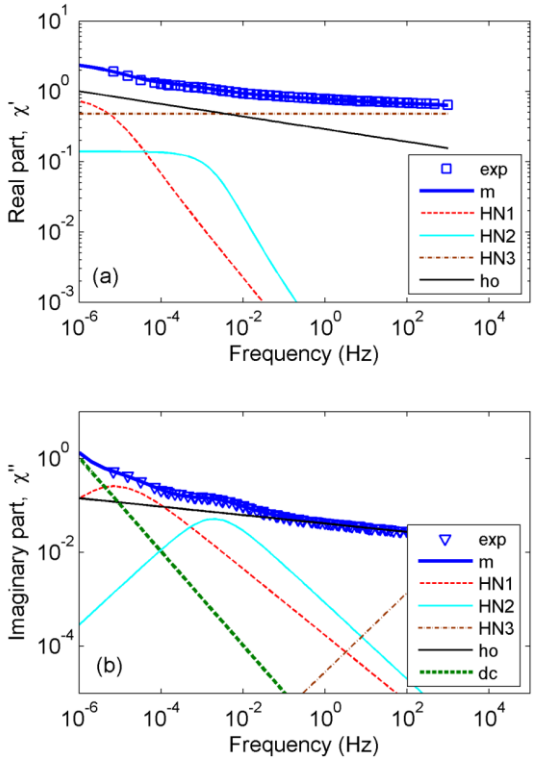


*Figure 2.12. Real (a) and imaginary (b) parts of the complex susceptibility of conventional enamel. The labels exp, m, HN, ho, dc represent the measured, modeled, Havriliak–Negami, hopping conduction, and dc conduction contributions, respectively.*

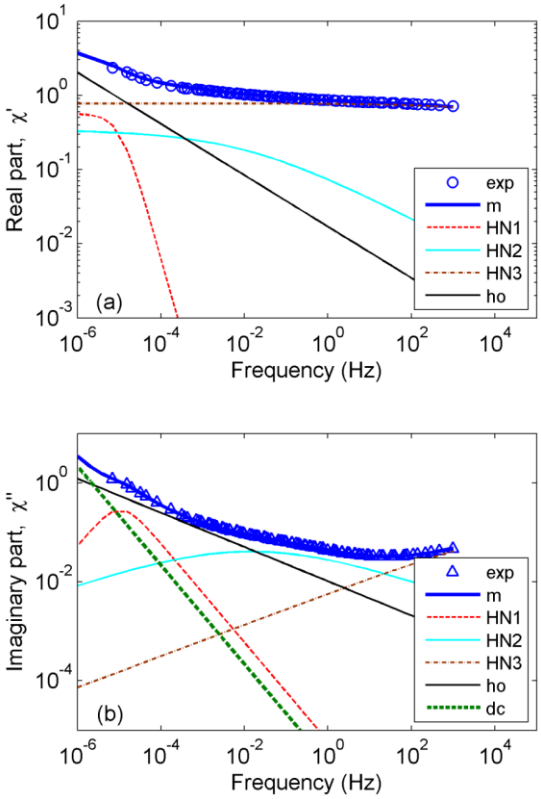


*Figure 2.13. Real (a) and imaginary (b) parts of complex susceptibility of filled enamel.*

in polymeric materials. Besides, the contribution of dc loss in the measured dielectric loss becomes considerable only at frequencies as low as $10^{-5}$ Hz.

In summary, the complex dielectric permittivity of the conventional enamel seems to be determined by the dipolar relaxation at high frequencies and MWS polarizations at the two interfaces in its multilayered structure at lower frequencies. The addition of chromium oxide fillers to enamel insulation gives rise to hopping conduction and MWS polarization at interfaces between the fillers and the base polymeric material. In addition, three relaxation processes present in the investigated enamel might have different activation energies, yet their value should be close to the results calculated in section 2.6.1. Otherwise, largely diffused master curves may be achieved [20]. Investigations should be further conducted to obtain more experimental evidences of relaxation processes in the insulation coating of the enameled wires.

## 2.7 Computer simulations

The influence of chromium oxide on dielectric properties of enamel insulation was studied using simulation tool Comsol Multiphysics©. A 3D model was created, representing the composite dielectric structure in Figure 2.3b. It consists of two layers corresponding to the base coat and the top coat, whose thickness is 25 and 15 μm, respectively. The top coat contained chromium oxide fillers of 8.7 vol%. Filler particles were considered as spheres of a diameter of 0.74 μm, regularly distributed in the base polymer. The size of the spheres was chosen as a statistical average based on the particle size distribution provided by the manufacturer. Since the dielectric properties of PAI and PEI differ slightly [8, 9], their characteristics could be ascribed to those of the conventional enamel. The measured complex permittivity of chromium oxide was also utilized for the simulations. All the input parameters for the model were taken from the experimental data obtained at 24 °C. The complex permittivity of filled enamel insulation was then calculated by the method proposed in [24].

The simulated and measured complex permittivities of the filled enamel are compared in Figure 2.14. A good agreement can be noticed in the losses, while a deviation ~7% is observed for the relative permittivity. The discrepancy may be attributed to the simplifications adopted in the simulations, e.g. considering fillers as spheres with identical diameters as well as their regular distribution in the polymeric insulation. It is notable that the measured and simulated relative permittivities are close to the values corresponding to Wiener's lower bound [25]. This fact reflects the similarity in physical processes in the considered layered system and in composite dielectrics containing series connection of their components. However, a substantial difference is that the top layer of the enamel insulation is a composite material itself. Although the significance of interfaces between fillers and polymeric matrix becomes less noticeable when the size of filler particles increases [26], their role cannot be ignored in microcomposites. The simulation results showed that relatively high localized electric fields appear inside the material at interfaces perpendicular to electric field lines. Surface charges are also accumulated in these locations as the continuity of the ration of $\varepsilon/\sigma$ is violated. Thus, electrical stress is enhanced at the interfaces, while it is weakened in the remaining part of the dielectric. This suggests that if PDs occur on wire surfaces of twisted pairs of the filled enamel, they are likely to erode the stressed interfacial regions close to the surfaces rather than the polymeric material. In other words, PD performance of twisted pairs is governed by the behavior of interfacial regions and the filler. Additionally, highly conductive fillers may allow for rapid dissipation of charges that limit damaging effects of PDs [27]. In contrast, the electric field is quite homogeneously distributed in the conventional enamel and PDs might erode any locations on wire surfaces, which results in enhanced

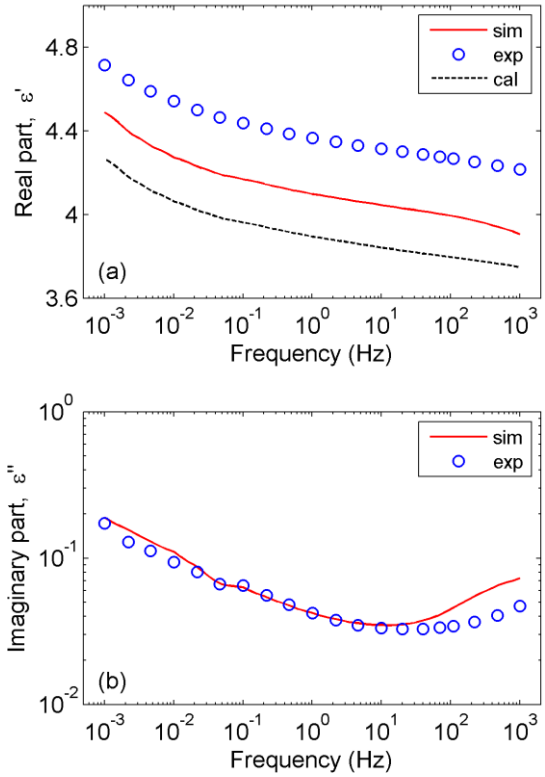


*Figure 2.14. Simulated (solid line) and experimental (circles) complex permittivity of filled enamel. Dashed line is for Wiener's lower bound of relative permittivity of laminar mixtures.*

deterioration and thus to premature failure of the insulation. In summary, the alternation of electric field distribution in the filled insulation can be considered as the dominating factor contributing to the increase of its life time as reported in recent investigation [7].

## 2.8 Summary

The dielectric properties of chromium oxide filled enamel were experimentally studied in a wide range of temperature and were compared with that of conventional enamel. Introducing relatively highly conductive and dispersive chromium oxide into the base polymeric material marginally increased the electrical conductivity of the enamel insulation. Furthermore, increasing temperature resulted in higher dc conductivity and dielectric loss; whereas it yielded lower relative permittivity. The use of the master curves allowed for analyzing the contribution of polarization relaxation processes in the investigated materials. The complex dielectric susceptibility of the conventional enamel was found to be primarily governed by the interfacial polarizations at low frequencies and dipolar relaxation at high frequencies. The presence of chromium oxide fillers in enamel insulation resulted in the appearance of interfacial polarization at their interfaces with the base polymeric material as well as in the increase of hopping conduction.

The simulated results of complex permittivity of filled enamel were consistent with the experimental data. It was noticed from the simulations that chromium oxide additives greatly altered the electric field distribution in the filled enamel, which might contribute to the improved PD resistance of filled enamel insulation.

# 3 Surface potential decay measurements

## 3.1 Surface potential measurements as a tool for material property characterization

Surface potential decay measurements have emerged as a powerful tool for characterizing properties of electrical insulating materials. Charges pre-deposited on material surfaces can decay due to several mechanisms such as charge injection followed by their transport in the bulk governed by volume conductivity (valid predominantly for electrons), dipolar polarization, surface charge leakage, charge neutralization by gas ions. A comprehensive review of the decay mechanisms can be found in [28, 29]. Specific mechanisms, which may be activated during the potential decay, depend strongly on material properties as well as experimental conditions. Thus, material properties can be revealed by analyzing the experimental results of surface potential decay.

For disorder solids, the evolution of surface charge/potential is largely controlled by the trapping and de-trapping of charges in localized states in material bulk. Traps existing in the materials may be occupied by charge carriers injected into the bulk. The energy depth of each trap controls the time duration that charges spend in the trap. Basing on this, Simmons and Tam [30] have proposed, and subsequently, Watson [31, 32] has developed the time-dependent de-trapping model by using the concept of demarcation energy level – the border between the filled and emptied localized states in disorder materials. Accordingly, the gap between the demarcation energy level $E_m$ and the extended state $E_0$ (the mobility edge for disorder states) is proportional to time passage $t$ since the injection event:

$$E_0 - E_m = kT \ln(\nu_0 t) \tag{3.1}$$

where $k$ is the Boltzmann constant, $T$ is the absolute temperature, $v_0$ is the attempt-to-escape frequency. The release of charge carriers from traps to the transport states results in the decay of surface potential d$V$/d$t$, and hence, the trap density at energy level $E_m$ is proportional to the product $t$d$V$/d$t$. Therefore, the plot of $t$d$V$/d$t$ versus log($t$) provides the image of trap density distribution in polymers that has been shown for e.g. polystyrene [31, 32] and polypropylene [33].

For insulating materials exposed to high electric field (~$10^7$-$10^8$ V/m), charge injection and transport has been considered as the main mechanism responsible for the decay of surface potential [34-39]. Numerous models based on charge injection and transport have been extensively employed for explaining experimental results of the decay process on thin films including the cross-over phenomenon firstly observed by Ieda and coworkers [40]. Sonnonstine and Perlman [35, 36] have proposed a model by making use of the concept of instantaneous partial injection or time dependent injection coupled with field-dependent mobility. Mathematical formulation of the model is based on Poisson's equation, continuity equation, and Ohm's law. Theoretical results derived by the proposed model show a good agreement with the experimental results previously obtained in [40]. In addition, the model

allows for obtaining charge carrier mobility in polyethylene. Further, von Berlepsch [37] has considered charge trapping and de-trapping in the early developed model by introducing a rate equation describing the variation of free charges and charges in deep traps. Hence, the model has been formulated by the transport equations consisting of Poisson's equation, continuity equation, and the rate equation in combination with the boundary conditions of electric field. Based on this, an analytical expression of time-dependent surface potential has been derived and utilized for fitting the experimental data. The model allows for revealing several transport parameters e.g. effective mobility in disorder states, hopping distance, trap concentration, and trap depth as well as trapping parameters e.g. the trapping rate and the release rate. In [41], the computer simulation utilizing the similar model has been implemented for analyzing the potential decay process on surface of polypropylene films. It has been shown that the simulated results are in good agreement with the experimental data only in case that the de-trapping of charges from traps is considered in the model.

Under certain circumstances, the removal of charges from insulation surface has been attributed to the intrinsic conduction [42]. Thus, the total effect of charge trapping and de-trapping can be summarized in term of the bulk conductivity of materials. The obtained bulk conductivity may exhibit the field-dependent behavior, thereby can be described by Poole-Frenkel model [43, 44]. The model has been utilized for characterizing electrical properties of several polymers such as EPDM and silicon rubber, whose thickness is in mm range. It has been noted that surface potential decay can be considered as an alternative method for evaluating material conductivity [45, 46].

The presence of electric field created by charges deposited on insulation surfaces may result in polarization relaxation processes in materials. This includes interfacial polarization as well as reorientation of dipoles existing in insulating materials. The interaction of the created bound charges inside the bulk and trapped surface charges results in the decay of surface potential. Dipolar polarization has been noted as the governing factor of surface potential decay for epoxy resin of 7 mm thick [47] and for thin films of high density polyethylene (HDPE) and polypropylene (thickness ~10 µm) [48]. The efficiency of the mechanism has been proved by showing a correlation between the decay rate of surface potential and the polarization displacement current. Additionally, Frederickson et al. [46] have developed a model based on dipolar polarization for fitting measured surface potential by using five parameters including the initial permittivity (at $t = 0$) and the permittivity at $t \rightarrow \infty$ of materials taking into account the effect of the bound charges at corresponding time instants.

## 3.2 Samples and experimental setup

### 3.2.1 Samples

Material samples used were created by winding enameled wires closely (turn to turn) around a wooden plate (100 mm × 50 mm × 6 mm) to form a winding of 40 turns, whose surface area is of 50 mm × 50 mm (Figure 3.1a). The use of winding samples in the present study allowed for emulating dynamics of charges deposited on motor winding surfaces due to PD activity.

Owing to the complicated geometry of the sample used, the effects of surface charges i.e. electric field in materials and the potential induced by deposited charges were calculated and compared with those corresponding to a flat sample (Figure 3.1b). The calculations were performed for samples of the conventional enamel utilizing Comsol Multiphysics software. It was assumed that in both systems, a surface charge with the of density of $10^{-6}$ C/m$^2$ was deposited on the gas-insulation interfaces, while the insulation-metal interfaces were grounded. As dielectric properties of layers of materials differ slightly, the enamel coating

was simulated as a single layer of 50 μm in thickness and having relative permittivity of 3.5 (close to the value measured at 1 kHz for the conventional enamel). Thus, the average calculated electric fields in the insulation were ~$3.3\times10^4$ V/m in both cases. The electric field profiles along straight lines perpendicular to the gas-insulation interfaces are provided in Figure 3.2. As can be seen, a small deviation (max. ~8.5%) was observed. In addition, the induced surface potentials were respectively 1.680 and 1.613 V for the winding and flat samples, yielding a discrepancy of 4.1%. Hence, the samples used in the present study (Figure 3.1a) can be considered using equivalent flat samples (Figure 3.1b) with the same insulation thickness. Therefore, experimental results obtained can be analyzed in the same way as for data received in an experimental setup with flat samples.

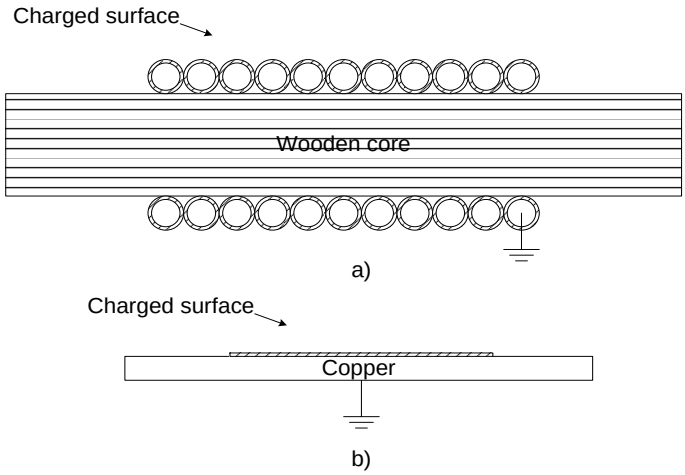


*Figure 3.1. Sample used in the experiments (a) and its equivalent representation by a flat layer of insulation on top of a grounded copper plate (b). The winding cross section is enlarged for clarity.*

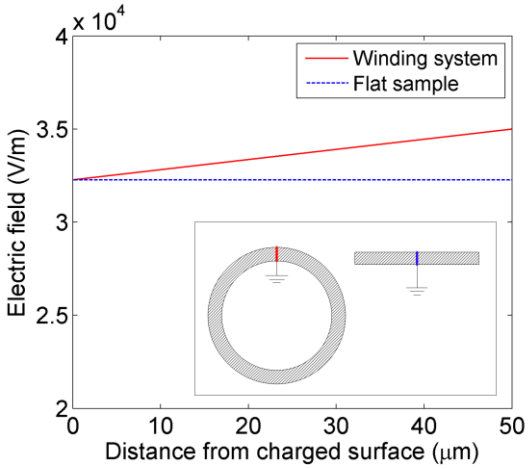


*Figure 3.2. Electric field in insulation of the winding and flat samples having a surface charge density of $10^{-6}$ C/m$^2$. The inset shows two samples as well as the directions along which electric field was calculated.*

### 3.2.2 Experiments

The experimental setup is shown schematically in Figure 3.3. The winding surface was charged by dc corona of either polarity created by a needle electrode kept at 4 mm above the winding center. The charging level varied from 3 to 4.5 kV. The sample was placed on a grounded copper plate (550mm $\times$ 800mm) and the wire conductor was always grounded during the experiments. Potential induced by charges deposited on winding surface was measured by a non-contact technique using Kelvin probe (vibrating reed probe) in connection with an electrostatic voltmeter (Trek 347). The probe (model 6000B-7C) was kept at 2 mm above the winding surface for optimizing the measurement ability. The obtained data were recorded using LabVIEW© software and stored for further analysis. A computer controllable motor system (XY Arrick Robotics) was utilized for positioning the needle and the probe. The experiments were conducted at room temperature (22 °C) and a stable level of relative humidity (30-35%).

A pre-scan was performed before each experiment to assure that the residual surface potential of the sample used was negligible. The experiment was initiated by corona charging the sample surface during two minutes. After charging, the needle electrode and the probe were relocated to the predefined positions for starting surface potential measurement. The potential distribution on the sample surface was obtained by moving the probe along the surface and across its center. After the measurement, the winding surface was grounded for a long period of time for neutralizing the remaining surface charges, thus preparing it for the next measurement. Each experiment was repeated three times and good reproducibility was achieved.

## 3.3 Surface charge density

The surface potential distribution for the conventional enamel obtained at 30 min after charging is shown in Figure 3.4a (charging voltage +4 kV). The scanning time was ~3.5 min. The bell-like shape of surface potential distribution was observed: the highest potential was at the sample center, where the charging needle was located, and it decreased gradually as the distance from the center increased. The potential distribution indicated the absence of back discharges which might develop from the deposited charges to the grounded needle immediately after completing the charging process [29].

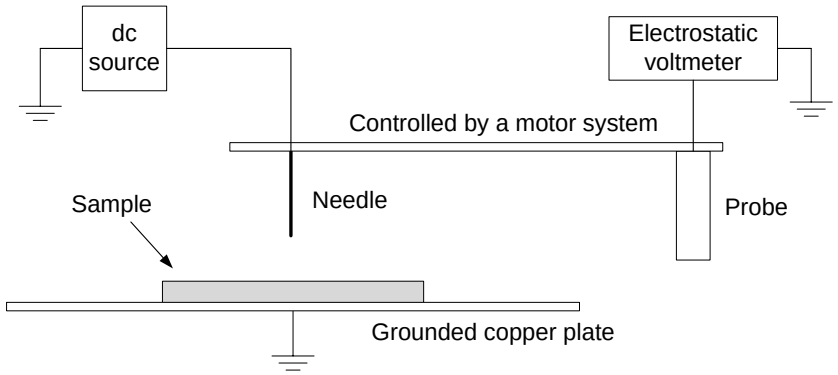


*Figure 3.3. Schematic arrangement of the experimental setup.*

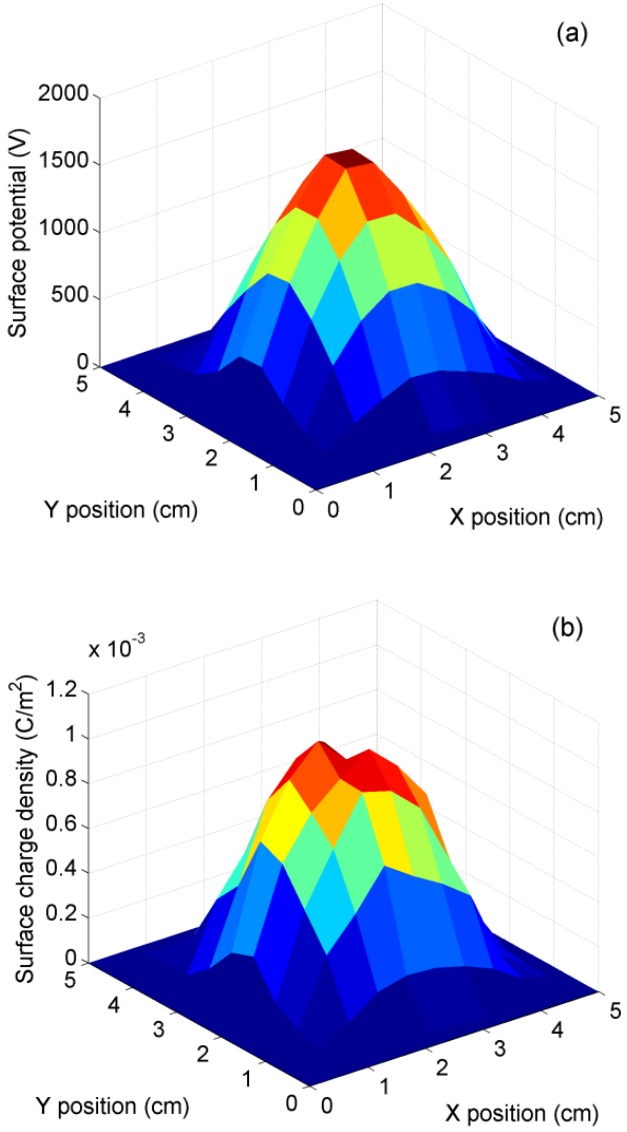


*Figure 3.4. Measured surface potential distribution (a) and calculated surface charge density (b) for conventional enamel at 30 min after corona charging of +4 kVdc.*

The obtained profiles of the surface potential can be converted to corresponding distributions of densities of surface charges assuming that the charge injection into the bulk is insignificant and, thus, the induced potential is mainly caused by surface charges. In case of homogeneous surface potential distribution, the surface charge density $\sigma_s$ can be directly derived from the measured surface potential $V$ by using Gauss's law as

$$\sigma_s = \frac{\varepsilon_0 \varepsilon_r}{d} V \tag{3.2}$$

where $\varepsilon_0$ is the vacuum permittivity, $\varepsilon_r$ is the relative permittivity of material, $d$ is the sample thickness. In this study, however, the corona charging from the needle electrode resulted in inhomogeneous potential distribution on sample surface, thus leading to the appearance of tangential electric field component. Hence, equation (3.2) is not applicable and charge density distributions can be obtained by employing Φ-matrix method [49]. For this purpose, the

sample surface was divided into 10×10 square elements with the side of 5 mm. The probe voltage $V_{ij}$ at position ($i$, $j$) was expressed as [49]

$$V_{ij} = \sum_{y=1}^{10}\sum_{x=1}^{10}\phi_{ij}(xy)\cdot\sigma_{xy} \tag{3.3}$$

where $\phi_{ij}(xy)$ represents the response function of the probe at position ($i$, $j$) to charge density $\sigma_{xy}$ at position ($x$, $y$), $1 \le x, y, i, j \le 10$. Equations (3.3) established for all probe positions ($i$, $j$) constituted an equation system that can be rewritten in the matrix form:

$$\mathbf{V} = \mathbf{\Phi}\boldsymbol{\sigma}_\mathbf{s} \tag{3.4}$$

where $\mathbf{V}$ and $\boldsymbol{\sigma}_\mathbf{s}$ denote vectors of surface potential and surface charge density, $\mathbf{\Phi}$ is a matrix containing all the response functions $\phi_{ij}$ of the probe. Consequently, the surface charge density can be found as

$$\boldsymbol{\sigma}_\mathbf{s} = \mathbf{\Phi}^{-1}\mathbf{V} \tag{3.5}$$

The matrix $\mathbf{\Phi}$ was obtained by means of computer simulation using Comsol Multiphysics©, similarly to that in [50]. A 3D model was created to simulate the measurement system, in which the winding structure was replaced by a flat sample, as pointed out in the previous section. Surface potential at each square element was gained by averaging the experimental results obtained by scanning. In the simulations, surface charge density of a certain square element at position ($x$, $y$) was assigned to a non-zero value, while surface charge density was zero at all remaining elements. At the same time, the probe was located above a specific position ($i$, $j$). The non-contact measurements in the experiments utilized so-called field nullifying technique (the potential of the probe body is the same as the potential at the measuring point on the surface). This was implemented in the simulation by varying the probe potential unless the electric field between the probe and the surface below was equal to zero. For this, the probe potential was assigned to a set of values in the parametric sweep option provided by the software, which was run continuously until the zero-field condition was achieved. The last value of the probe potential obtained in this procedure was used for calculating the corresponding response function $\phi_{ij}(xy)$ of the probe by utilizing (3.3). The variation of parameters $x$, $y$, $i$, $j$ from 1 to 10 was achieved by employing additional parametric sweeps. After attaining all the probe's response functions in the matrix $\mathbf{\Phi}$, surface charge density was obtained from expression (3.5). The results of the calculations are demonstrated in Figure 3.4b. The bell-like shape of surface charge distribution was also obtained, even though two localized peaks were observed. The maximum surface charge density was ~1.0 mC/m$^2$, whereas the total amount of surface charges was ~740 nC in this particular circumstance. The obtained results of surface charge density were then compared to that calculated by equation (3.2), which is shown in Figure 3.5 for a line across the center. As the discrepancy between results obtained by the two methods was small (max. 12%), equation (3.2) provides an acceptable approximation of surface charge density. Thereafter, instead of obtaining 2D potential distribution on the whole surface, the 1D potential profiles along two straight lines (parallel and perpendicular to wires) across the surface center will be sufficient for presenting the potential distribution for the considered samples.

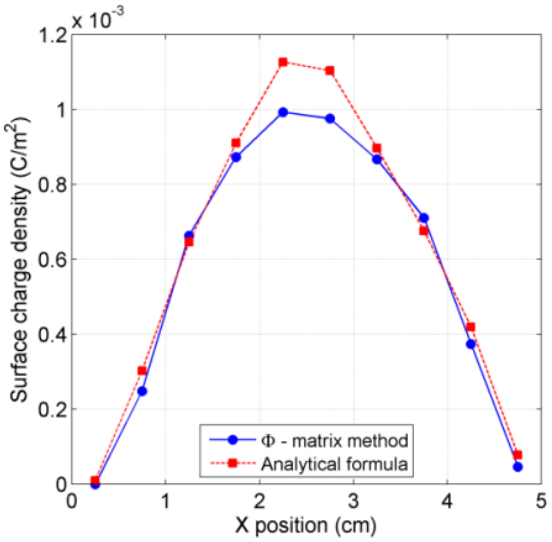


*Figure 3.5. Surface charge density along the direction parallel to X axis (Y = 2.5 cm) and across the sample center calculated by Φ-matrix method and by equation (3.2).*

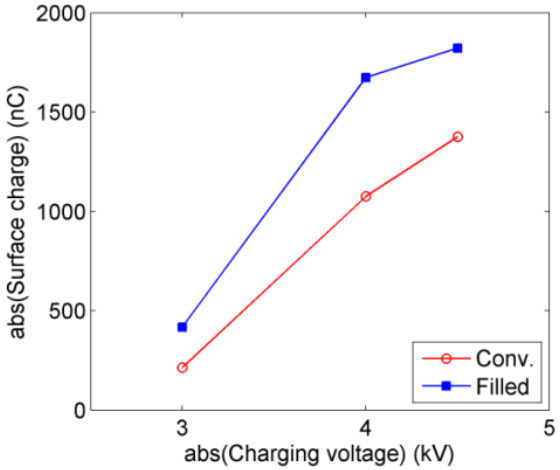


*Figure 3.6. Total surface charges recorded at 3 min after charging by negative corona.*

The total amount of surface charges at 3 min after charging, obtained by surface integration of the calculated charge density, is shown in Figure 3.6 for negative corona charging. A larger amount of surface charges was recorded for the filled enamel than for the conventional one, which might be due to the difference in the intensity of corona charging for two materials. Enhancing the charging voltage magnitude from 3 to 4 kV led to a rapid increase in the amount of deposited charges, thereafter the rate of rise was slower.

## 3.4 Surface potential decay

### 3.4.1 Initial surface potential

As will be revealed in section 3.4.2 the surface potential distribution is symmetrical about the sample center, hence it can be represented by the potential profile in direction along the wires and across the sample center. Surface potential distribution measured at 3 min after charging for the filled enamel at different charging levels is shown in Figure 3.7. The bell shape of the distribution was always observed, in which the potential was highest at the sample center

where the corona needle was located during charging. The radius of the charged spot increased with the charging voltage, indicating more charges deposited on sample surface. A polarity effect is also notable in the characteristics. For example, the lowest charging level for negative polarity at –3 kV yielded a charged spot of 1.5 cm in radius and maximum potential of –1500 V. Meanwhile, the charging conducted at the same voltage magnitude for positive polarity did not result in charge deposition. By increasing the charging level to +3.5 kV, a similar amount of surface charges deposited as for the charging voltage of –3 kV was achieved. In addition, at the other two charging voltages (4 and 4.5 kV), the maximum surface potential obtained was higher in case of negative polarity than for positive polarity. This can be attributed to a known fact that corona discharges in a needle-plane configuration are stronger at negative polarity as compared to that at positive polarity [51].

### 3.4.2 Decay on winding samples

As the surface potential and the surface charge density are approximately correlated by equation (3.2), the decay of the latter can be demonstrated by that of the former. Figure 3.8 illustrates the surface potential decay of the filled enamel for the charging voltage of –4 kV in two directions (perpendicular to enameled wires and along them). The difference in sample geometry in the two directions suggests that surface charge leakage is more likely to appear along wires rather than in direction perpendicular to them (the turns of the wires in the sample are separated by small air gaps). However, as can be seen from the figure, similar shapes of surface potential distribution are observed for the two directions and lateral spreading of surface potential is not observed, implying a weak charge transport along insulation surface. In other words, surface charge leakage did not play an important role in charge decay. Apart from surface leakage, surface charges could decay through bulk transport and charge neutralization by gas ions available in air volume nearby [43]. Taking into account that the experiments were conducted in such a way that zero field was maintained between the probe and the charged surface, negligible gas neutralization can be assumed for the surface part underneath the probe (note that the radius of the probe body was ~11.2 mm). Consequently, bulk neutralization can be suggested as a main process causing surface charge decay. Note

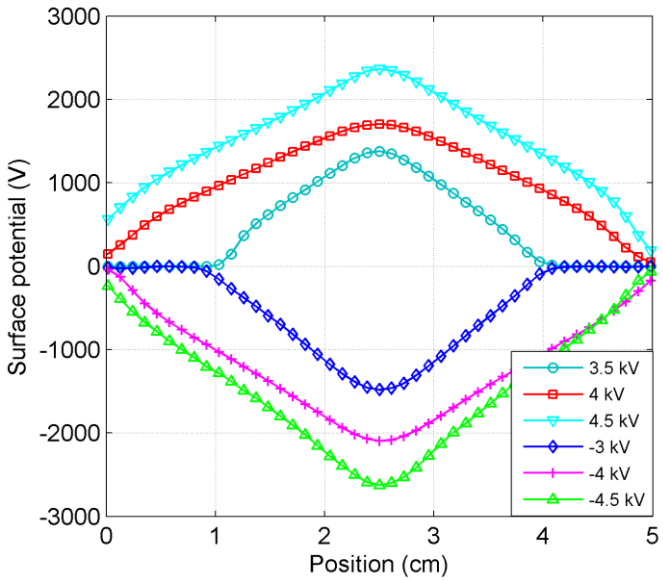


*Figure 3.7. Surface potential distribution at 3 min after charging. The charging needle was placed at 2.5 cm.*

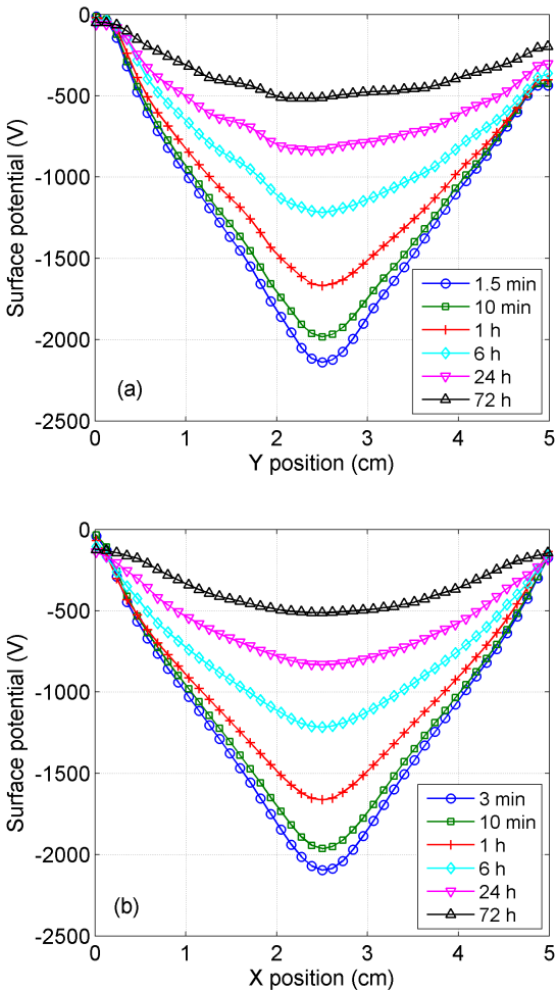


*Figure 3.8. Surface potential distribution for the filled enamel charged by negative corona (–4 kV) in two directions across the surface center: perpendicular to wires (a) and along wires (b).*

also that surface potential decayed faster at the sample center (where the potential was higher) than at its edges that indicates a field-dependent decay behavior. Finally, the surface potential distributions were similar for the both investigated enamels and, therefore, the results for the conventional enamel are not presented, but all the above remarks are also applicable.

### 3.4.3 Decay process at sample center

The results of potential decay at the sample center for both insulating materials are shown in Figure 3.9 for negative charging voltage. Note that the initial magnitudes of the surface potentials were recorded at 10-20 s after charging. Data presented here are normalized by dividing the measured results to their initial values. As can be seen, the potential decay process was faster for the filled enamel than for the conventional alternative. For example, at charging level of –4 kV, the decay of surface potential to 50% of its initial level required $\sim 3\times 10^4$ s for the filled enamel, while it took $\sim 3\times 10^5$ s (ten times longer) for the conventional enamel. In general, the decay process was accelerated as the charging voltage increases, showing the dependence of the decay rate on the surface potential magnitude. The decay of the normalized surface potential was slightly differed when the polarity of the charging voltage changed, but the main features were preserved, therefore that of positive polarity is not shown here.

The dependence of the decay rate on surface potential is illustrated in Figure 3.10 for the charging voltage of –4 kV. As seen, the rates were almost equal at the beginning of the decay process (high potential values) and it was around one order of magnitude higher for the filled enamel than for the conventional enamel at the end of the decay process. The observed difference in the decay rate could be due to the properties of chromium oxide filler. From the figure, it is evident that for both materials the decay rate exponentially reduced with decreasing surface potential (the experimental data can be fitted by a straight line in the semi-logarithmic scale used). Recalling for the analysis of the possible decay mechanisms above, this implies a field dependence of the "apparent bulk conductivity" which has to be accounted for in the decay model based on intrinsic conduction.

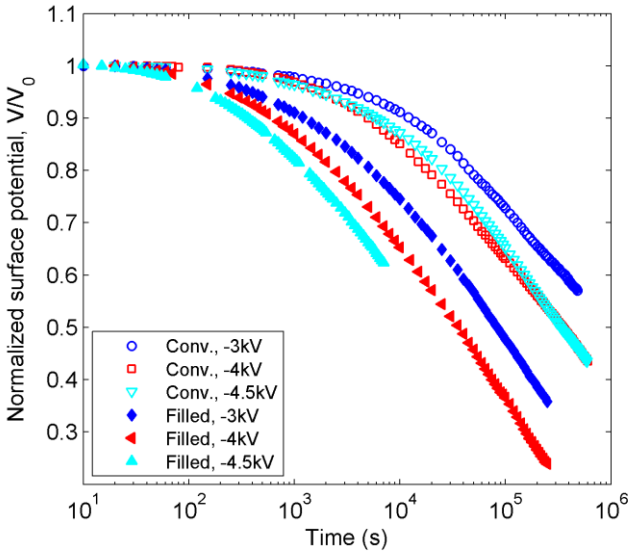


*Figure 3.9. Decay of normalized potential at the center of winding surfaces. Charging voltages are indicated in the legend.*

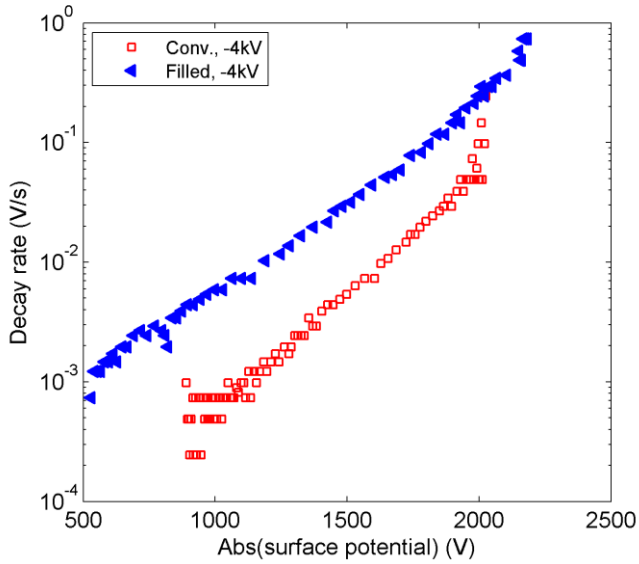


*Figure 3.10. Decay rate of surface potential at the center of winding surfaces at charging level of –4 kV.*

Time dependencies of the decay rate can be treated differently. Thus , Figure 3.11 presents the normalized decay rate d$V/V_0$d$t$ as a function of time in the log–log plots for the filled enamel charged by positive corona (+4.5 kV). Here, the time derivative was calculated for the normalized surface potential $V/V_0$. An important feature on this plot is that the normalized decay rate d$V/V_0$d$t$ can be fitted by two straight lines with different slopes, thereby it can be described by the power-law dependence on time as

$$-\frac{dV(t)}{V_0 dt} = \begin{cases} M_1 \cdot t^{-(1-\alpha_1)} & t < t_T \\ M_2 \cdot t^{-(1+\alpha_2)} & t > t_T \end{cases} \tag{3.6}$$

Here $M_i$ is a constant, $\alpha_i$ is a power factor, $t_T$ is the characteristic time corresponding to the knee point of the curve. The factors $\alpha_i$ obtained at different initial potentials are provided in Figure 3.12. As seen, these parameters varies within narrow intervals and their weak dependences on the field strength are illustrated by the fitting curves. This observation is similar to that reported in [37] for the surface potential decay on thin HDPE films. The characteristic times $t_T$ vary between 1000 and 2000 s, and no field dependence is noted for this parameter.

For the conventional enamel, the normalized decay rate also obeys the power-law dependence. The factors $\alpha_i$ obtained by curve fitting are presented in Figure 3.13. It should be noted that the tendency of the field dependences of $\alpha_i$ is different for the two materials. For example, $\alpha_2$ is higher at stronger initial electric fields for the filled enamel, while the opposite tendency is observed for this parameter in case of the conventional enamel. Furthermore, the characteristic time $t_T$ varies in a wider range, between 3000 and $10^4$ s.

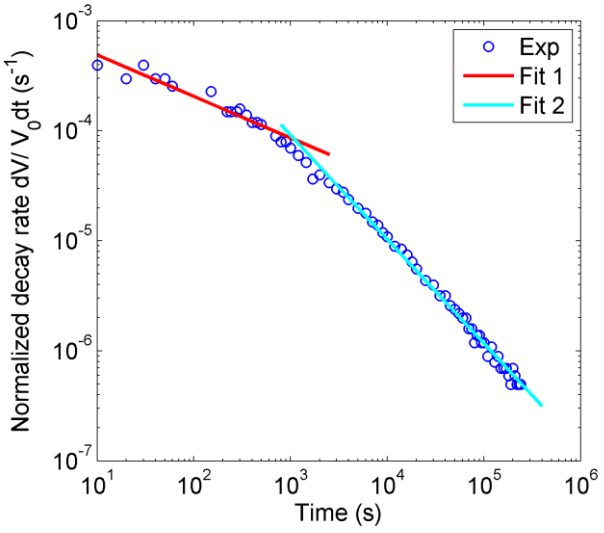


*Figure 3.11. Decay rate of normalized surface potential for filled enamel charged by positive corona (+4.5 kV).*

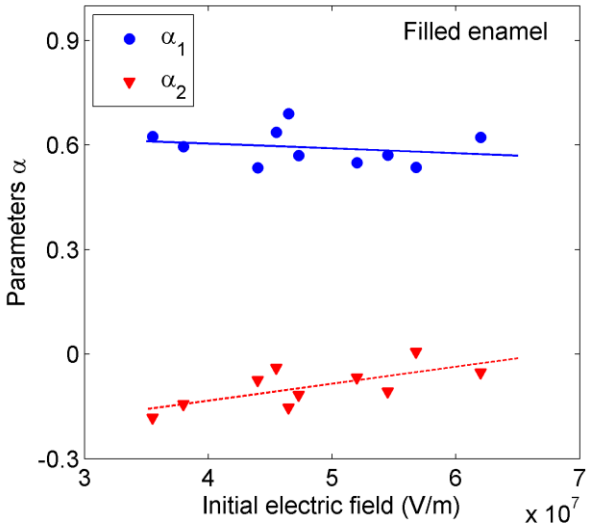


*Figure 3.12. Decay parameters α as functions of initial electric field for filled enamel.*

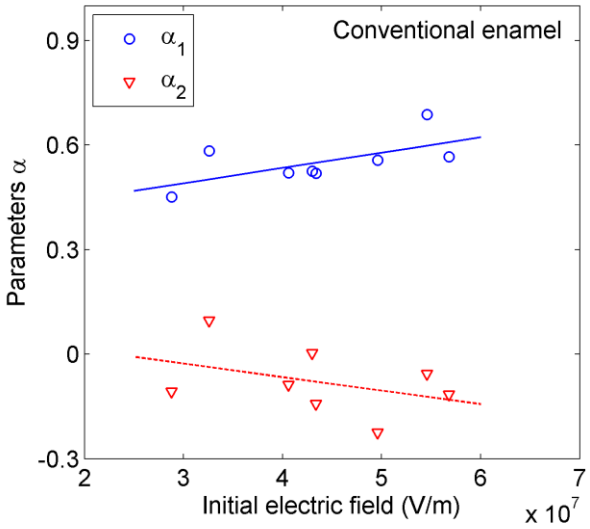


*Figure 3.13. Decay parameters α as functions of initial electric field for conventional enamel.*

The small variations in the values of the power factors $\alpha_i$ as well as of the parameters $M_i$ for each material suggest that the normalized decay rate tends to be a unique function of time, irrespectively of the initial surface potential $V_0$ and the polarity of the charging voltage. Thus, it may be related to the polarization displacement current as described by the model based on dipolar polarization [47]. Besides, the power-law dependence of the decay rate indicates that charge injection may contribute to the decay process [37, 38]. Accordingly, the results on surface potentials obtained in this experimental study are examined further (section 3.5) utilizing corresponding models.

### 3.4.4 Potential decay process on single-layer insulation

This section provides results of surface potential decay measurements conducted with single-layer enamel insulation. The obtained data are then used for comparison with the decay process on the multilayered enamel coatings reported above. The experiments were conducted

for the two flat samples previously used for the dielectric measurements presented in section 2.2. Surface charging (positive corona, +4 kV) and surface potential monitoring were performed according to the procedure described in section 3.2.

For the PAI layer, the bell-like shape of surface potential distribution was obtained. The initial surface potential recorded at the sample center was 1.3-1.5 kV. The density of the deposited surface charges, estimated by equation (3.2), was on the same level as for the winding samples. The measured potential decay characteristic and the decay rate at the sample center are provided in Figures 3.14 and 3.15, respectively. As seen, the decay process was very fast for the single-layer of PAI: the potential dropped to 50% of its initial value just in ~150 s. The decay rate shows a power-law dependence with a knee point at ~70 s.

In contrast, a saddle-like shape of the surface potential distribution was observed for the filled PAI insulation as shown in Figure 3.16. This indicates the appearance of a back discharge, which is probably due to overcharging. However, reduction of the charging time to 90 s and 60 s (for avoiding overcharging), did not change the appearance of the distribution. One may also notice much lower magnitudes of the surface potentials as compared to the previous case. It is not meaningful to compare surface potential magnitudes for these samples as their thicknesses and dielectric properties are different. Instead, the surface charge density should be reconstructed utilizing equation (3.2) prior to performing any comparison. For this, the value of relative permittivity of the filled PAI insulation has been estimated by computer simulation using the model of composite dielectric similar to that described in section 2.7. The simulation showed that the increase in relative permittivity of the $Cr_2O_3$-filled layer (with filler content of 4.3 vol%) compared to the PAI sample was not significant (~13%) as the filler content is far below the percolation level. The maximum surface potential measured at 90 s after charging for both the flat samples and the corresponding surface charge density are provided in Table 3.1. As seen, the maximum surface charge density recorded for the $Cr_2O_3$-filled PAI insulation at that time instant amounts to 75% of that for the PAI layer. The observation may be attributed to the faster decay of surface charges of the filled material as compared to that of the PAI layer (which will be exhibited in Figure 3.17). It should be noted that the localized peaks in potential distribution of the filled PAI were observed at locations of ~1 cm apart from the surface center, whose charge density is expected to be lower than that at the center in case of absence of back discharge.

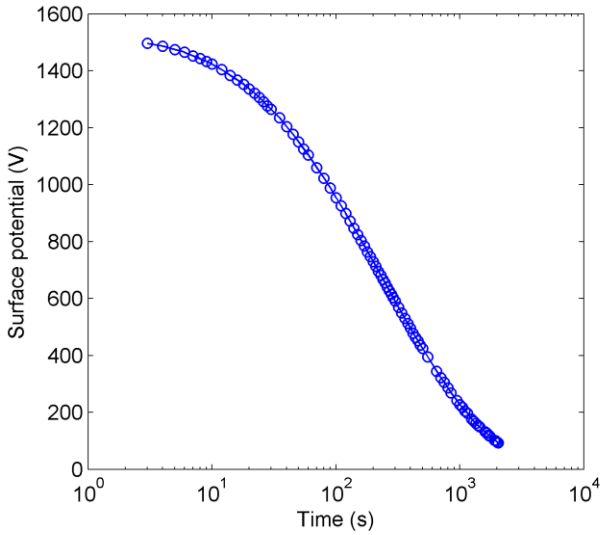


*Figure 3.14. Decay of surface potential at the center of PAI layer.*

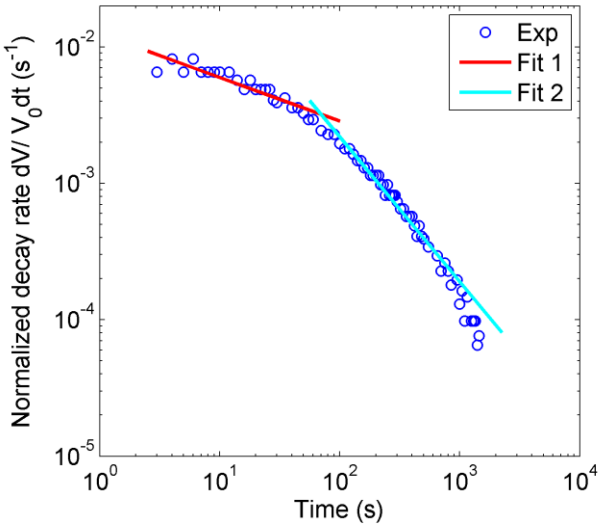


*Figure 3.15. Decay rate of normalized surface potential at the center of PAI layer.*

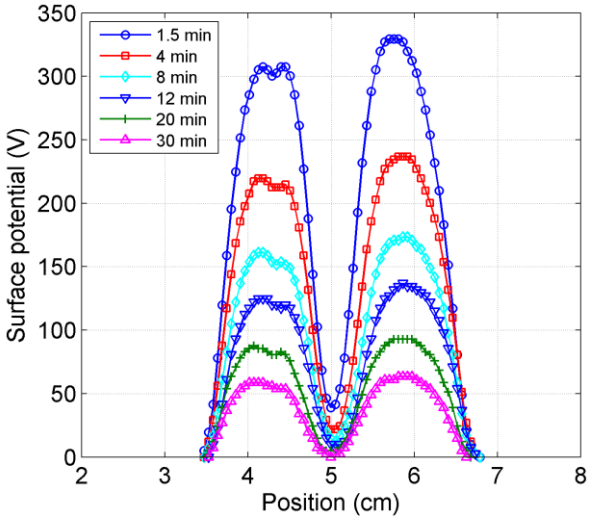


*Figure 3.16. Surface potential decay for the single layer of $Cr_2O_3$-filled PAI (charging time 90 s).*

*Table 3.1. Maximum surface charge density on flat samples at 90 s after charging*

| Sample | Thickness, µm | Max. surface potential, V | Charge density, $C/m^2$ |
|---|---|---|---|
| PAI | 38 | 989 | $0.8\times10^{-3}$ |
| $Cr_2O_3$-filled PAI | 19 | 332 | $0.6\times10^{-3}$ |

The results obtained for single layers of the materials (flat samples) are found to be quite different from the results measured on the filled insulation of the enameled wire. The latter consists of a PEI base coat and a top coat of PAI filled with $Cr_2O_3$ at 26 wt%, whose thickness is of ~25 and ~15 µm, respectively. The material of the base coat (PEI) was not available for

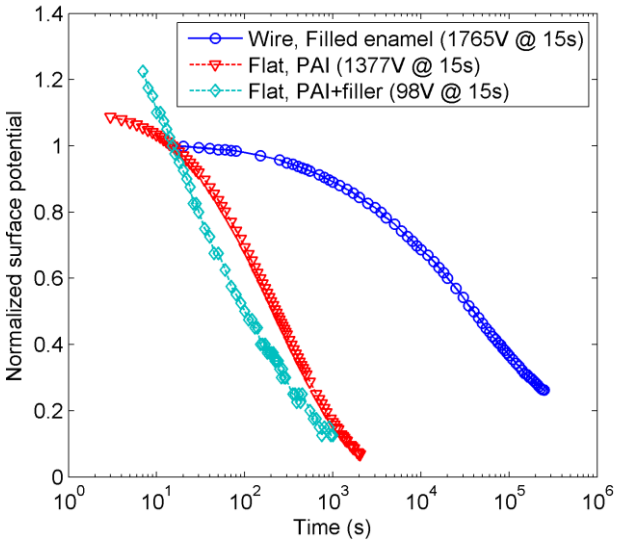


*Figure 3.17. Potential decay at the center of sample surface for the filled enamel and single layers of PAI and $Cr_2O_3$-filled PAI resins.*

doing surface potential measurements, however as discussed in chapter 2, electric conductivity of PEI is in two orders lower than that for PAI, therefore, the decay of surface potential should be slower for the former as compared to that of the latter. In contrast, similarity should be considered in the potential decay process for top coat of the filled enamel and the $Cr_2O_3$-filled PAI layer used owing to the closeness in their thickness and filler content. Thus, a plot providing comparative results of potential decay for the filled enamel and the two single-layer insulations used (Figure 3.17) might be helpful for explaining the decay mechanism, even though the flat samples used do not have the same filler content as for the constituents of the filled enamel. Note that the surface potential at sample center was strongly reduced for the $Cr_2O_3$-filled PAI due to the appearance of back discharge. Therefore, the data should be normalized by dividing the measured results to the potential at 15 s after charging. As can be seen, the potential decay process was far slower for the filled enamel than for the single-layer samples used. For instance, the surface potential decay to 50% required less than 300 s for the single layers, while it appeared at $\sim 3\times 10^4$ s for the two-layer filled insulation. For the PEI insulation (with an identical thickness as for the PAI layer used), the time to half of the initial potential is assumed less than the corresponding for the filled enamel. The slow decay process of the filled enamel could only be explained by the contribution of the interface between two layers to the decay process, which will be discussed in the following section.

## 3.5 Surface potential decay mechanisms

The decay of charges deposited on insulation surface is usually measured in an open circuit configuration by means of non-contact technique. Neglecting the influence of the free ions in gas surrounding charged surface, the decay of the induced surface potential can be analyzed based on a current continuity equation, which can be represented in the form [28]

$$\frac{\partial D}{\partial t} + \sigma E + \sum_i \mu_i \rho_i E = 0 \tag{3.7}$$

The first term represents the polarization of material exposed to the electric field $E$ induced by deposited charges, where $D$ being the displacement field. The second term is related to the intrinsic conduction $\sigma$ of material due to the field $E$. The third term takes into account the dynamic of charges injected into the insulation, where $\mu_i$ and $\rho_i$ are the mobility and charge density, respectively. The contribution of each mechanism on the total decay of surface charges depends on several factors such as dielectric properties of materials as well as the magnitude of electric field in the sample.

In order to understand the physical mechanism of surface charge decay, numerous models have been proposed. A brief analysis of potential decay models accounting for intrinsic conduction, dipolar polarization, and charge injection is provided here and is utilized further for examining the experimental results of surface potential decay.

### 3.5.1 Intrinsic conduction

The dominance of the intrinsic conduction is found in case when polarization becomes stabilized and the effect of injected charges is insignificant. Hence, the third component in the continuity equation can be ignored, and the apparent bulk conductivity can be derived as

$$\sigma(V) = -\frac{\varepsilon}{V(t)}\frac{dV(t)}{dt} \tag{3.8}$$

where $V(t)$ is the surface potential as a function of time, $\varepsilon$ is the of material permittivity (which is a constant value for stabilized polarization). Note that (3.8) is obtained assuming that the field in the material bulk induced by the surface charges is uniform $E = V(t)/d$, where $d$ stands for the sample thickness.

For insulating materials, the bulk conductivity can be attributed to hopping transport of charge carriers between trapping centers existing in the bulk. Such conduction model has been used for characterizing the electrical properties of several insulating materials such as EPDM and silicon rubber. Since the apparent bulk conductivity appears to be field-dependent [44], it can be introduced in terms of Poole–Frenkel model as a function of $\sqrt{V}$:

$$\sigma(V) = \sigma_c \exp(\beta_{PF}\sqrt{V}) \tag{3.9}$$

where the theoretical Poole–Frenkel coefficient $\beta_{PF}$ is defined as

$$\beta_{PF} = \frac{q}{kT}\sqrt{\frac{q}{\pi\varepsilon d}} \tag{3.10}$$

Here, $\sigma_c$ is a constant parameter, $k$ is the Boltzmann constant, $T$ is the absolute temperature, $q$ is the elementary charge.

In the present study, field-dependent behavior is observed for the apparent bulk conductivity for both the enamels (Figure 3.18). The obtained conductivity was higher for the filled enamel than for the conventional one, which is associated with the rates of the decay processes on the sample surfaces. The addition of conductive chromium oxide into the top coat obviously gave rise to the bulk neutralization of charges in the filled enamel. As the slopes of the volume conductivity curves changed, the obtained characteristics can be separated into two regions, parameters of which are provided in Table 3.2. In region I, the strong field dependence of the apparent volume conductivity is observed for both enamels and it is underestimated by Poole–

Frenkel model ($\beta_I > \beta_{PF}$). Since thin layers of enamels used in experiments were exposed to strong electric fields (~$4\times10^7$ V/m), charge injection and transport as well as dipolar polarization can be suggested as dominating mechanisms contributing to surface charge decay on the studied materials in the initial stage [28]. In region II, as the surface potential reduced, the field dependence of the volume conductivity weakens in both materials, and it is overestimated by Poole–Frenkel model ($\beta_{II} < \beta_{PF}$). The conductivity at surface potential of 100 V can be extrapolated by assuming that it follows the field dependence with a constant slope ($\beta_{II}$) at low surface potentials. As seen from Table 3.2 for both materials, the results calculated by this procedure are in two orders lower than the volume conductivities measured by the standard method (recall, however, that in the latter case transient currents measured at $10^5$ s were utilized as discussed in chapter 2). The volume conductivities of enamels might appear to be field-independent even in weak electric fields (region II), as shown by the horizontal dashed lines in Figure 3.18. Thus, the field-independent conductivity can be attributed to the intrinsic conduction, whereas the strongly field-dependence behavior could

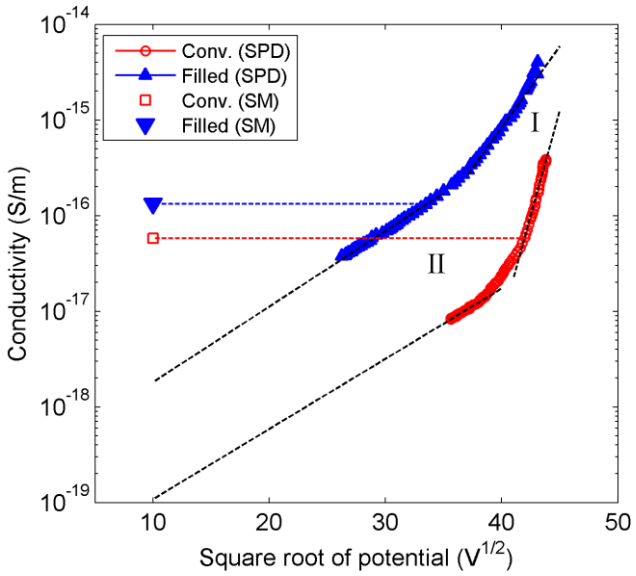


*Figure 3.18. Field-dependent volume conductivity of enamels derived from surface potential decay measurements (SPD) at charging voltage of 4 kV. Dashed straight lines with different slopes are added in two regions. The volume conductivities measured by the standard method (SM) are also provided for comparison.*

*Table 3.2. Parameters of field-dependent model for the studied materials*

| | Conventional enamel | Filled enamel |
|---|---|---|
| Slope in region I, $\beta_I$ | 1.013 | 0.390 |
| Slope in region II, $\beta_{II}$ | 0.169 | 0.182 |
| Poole–Frenkel coefficient calculated by (3.9), $\beta_{PF}$ | 0.245 | 0.254 |
| Extrapolated volume conductivity at 100V, S/m | $1.08\times10^{-19}$ | $1.81\times10^{-18}$ |
| Measured volume conductivity at 100V, S/m | $5.80\times10^{-17}$ | $1.33\times10^{-16}$ |

be due to space charge limited current. One may argue that surface potential decay measurements should also be carried out at lower initial potential levels (several hundred volts) for obtaining the apparent volume conductivity. Those experiments, however, yielded an unstable potential decay process and poor reproducibility, which might be due to the winding structure of the samples used. In summary, the electrical conductivities of the studied materials are strongly field-dependent, but they do not obey the Poole–Frenkel model.

If the decay process is mainly governed by intrinsic conduction of material, a single value of conductivity should be obtained for a certain surface potential, independently of the data used for calculations. In other words, the curves of the apparent bulk conductivity derived from different charging voltage magnitudes must overlap each other. As can be observed in Figure 3.19, it is not the case for the present study. This suggests that the third component in the equation (3.7) cannot be ignored and intrinsic conduction is not the major contribution to the decay process.

Discrepancies in the apparent bulk conductivity of the studied materials can also be found if surface potentials measured at different locations on sample surface are utilized. Thus, the results shown in Figure 3.20 present the bulk conductivity obtained from decay characteristics for three different locations apart from the sample center. As seen, the deviations from the data corresponding to the central point increase with increasing distance from the center that can be correlated with the reduction of the magnitude of the surface potential and, hence, the induced field.

The obtained results imply that the apparent conductivity includes contributions of several mechanisms to the bulk neutralization, such as intrinsic conduction, dipolar polarization as well as charge injection and all of them cannot be ignored. The contribution of intrinsic conduction becomes important only at later stages of the decay process when polarization is stabilized and the dynamics of injected charges is weakened. This argument is supported by the fact that the bulk conductivity derived at this stage is comparable to the parameter measured by the standard method provided in chapter 2.

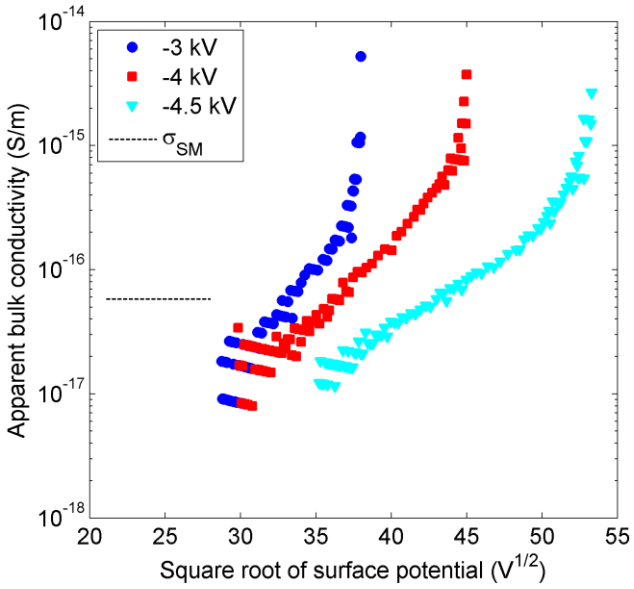


*Figure 3.19. Field-dependent bulk conductivity of the conventional enamel derived from results of surface potential decay for three charging levels marked in the legend. The bulk conductivity measured by the standard method is marked by the horizontal line.*

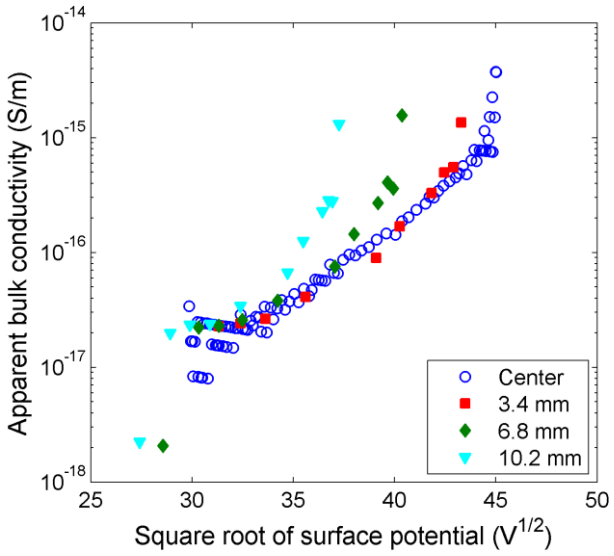


*Figure 3.20. Field-dependent bulk conductivity of the conventional enamel derived from results of surface potential decay at charging voltage of –4 kV for the sample center and three locations on the surface (distances from the center are indicated in the legend).*

## 3.5.2 Dipolar polarization

### 3.5.2.1 Background

Charges deposited on insulation surface create an electric field inside the material that may stimulate the alignment of dipoles existing in polymer as well as interfacial polarization in the material, thus causing the formation of bound charges inside the insulation. Even though the density of free surface charges is constant [28], the interaction between bound charges and the deposited charges may result in the decay of surface potential. As can be noticed from the current continuity equation, the contribution of polarization to decay process largely depends on material properties. If the intrinsic conduction in a material is extremely weak and the injected charges are negligible, polarization relaxation processes may become the main factor affecting surface potential decay. One should note that the contribution of dipolar polarization to surface potential decay has not been commonly reported in literature. A possible reason for that might be either the use of materials with relatively high electrical conductivity in experiments thus increasing the role of intrinsic conduction, or the use of very thin samples (thickness is in μm range) within which high electric fields are induced thus promoting the role of charge injection and transport in the decay process. The role of dipolar polarization was systematically evaluated by Molinie and coworkers [28, 47, 48]. The authors derived [47] mathematical expressions relating the decay rate of surface potential and the polarization current. In [48], similarity was observed for the behavior of the time derivative of surface potential and the absorption current described by Curie – von Schweidler law, thus providing a theoretical support for the model based on dipolar polarization. In this work, we follow the mathematical treatment proposed by Molinie and coworkers to discuss the contribution of polarization to potential decay.

The applied electric field $E(t)$ and the displacement field $D(t) = \varepsilon_0 E(t) + P(t)$ (where $P(t)$ is the dielectric polarization) in dielectric materials can be related by a convolution [28]:

$$D(t) = \varepsilon_0 \int_{-\infty}^{t} E(\tau)\phi_D(t-\tau)d\tau \tag{3.11}$$

$$E(t) = \frac{1}{\varepsilon_0} \int_{-\infty}^{t} D(\tau)\phi_E(t-\tau)d\tau \tag{3.12}$$

Here, $\phi_D$ and $\phi_E$ are dependent functions, the product of their Laplace transforms being 1. By noting that $E = V/d$, the current and the decay rate of surface potential have been derived from (3.11) and (3.12) as [28]

$$i(t) = C_0 V_2 \phi_D(t) \tag{3.13}$$

$$\frac{dV(t)}{dt} = \frac{d \cdot q_0}{\varepsilon_0}\phi_E(t) \tag{3.14}$$

where $C_0$ being the geometrical capacitance of sample, $V_2$ is the applied voltage in the polarization current measurement, $d$ is the sample thickness, $q_0$ is the amount of surface charges deposited. By assuming $V_1 = d \cdot q_0/\varepsilon_0$, equation (3.14) can be rewritten as

$$\frac{dV(t)}{V_1 dt} = \phi_E(t). \tag{3.15}$$

In literature, the dielectric response function $f(t)$ is commonly employed to link the dielectric polarization $P(t)$ and the electric field $E(t)$ through a convolution relationship [52]:

$$P(t) = \varepsilon_0 \chi_\infty E(t) + \varepsilon_0 \int_{-\infty}^{t} f(t-\tau)E(\tau)d\tau \tag{3.16}$$

Comparing (3.11) and (3.16) and recalling $D(t) = \varepsilon_0 E(t) + P(t)$, one may obtain a correlation between the function $\phi_D(t)$ and the dielectric response function $f(t)$:

$$\phi_D(t) = (1+\chi_\infty)\delta(t) + f(t) = \varepsilon_\infty \delta(t) + f(t) \tag{3.17}$$

Here, $\chi_\infty$ and $\varepsilon_\infty$ are the dielectric susceptibility and permittivity at high frequencies, $\varepsilon_\infty = \chi_\infty + 1$, $\delta(t)$ is the Dirac function. Equation (3.17) implies that the shapes of $\phi_D(t)$ and $f(t)$ are identical, as noticed in [28]. Since it is assumed that materials have zero conductivity [28], the current $i(t)$ referred to in (3.13) is the displacement current. In reality, the current $i(t)$ can be obtained by subtracting the component due to intrinsic conduction $\sigma$ from the measured polarization current.

To verify the hypothesis that dipolar polarization is deterministic in the decay of surface potential, we rely on the correlation between the Laplace transforms of the functions $\phi_D$ and $\phi_E$. One can derive the following expression from (3.13) and (3.15):

$$\mathbf{L}\{C_0 \phi_D(t)\} \cdot \mathbf{L}\{\phi_E(t)\} = \mathbf{L}\left\{\frac{i(t)}{V_2}\right\} \cdot \mathbf{L}\left\{\frac{dV(t)}{V_1 dt}\right\} \tag{3.18}$$

where operator **L** denotes the Laplace transform. Equation (3.18) can be rewritten:

$$C_0 = \frac{1}{V_2}\mathbf{L}\{i(t)\} \cdot \mathbf{L}\left\{\frac{dV(t)}{V_1 dt}\right\} \tag{3.19}$$

In summary, if the relationship (3.19) is fulfilled for the decay rate of surface potential d$V$/d$t$ and the displacement current $i(t)$, dipolar polarization can be considered as the main reason for the decay of surface potential.

#### 3.5.2.2 Examining experimental results by the model based on dipolar polarization

To confirm the influence of dipolar polarization on surface potential decay, the right hand side of (3.19) is calculated for measured data. Since $V_1 = d \cdot q_0/\varepsilon_0$ being the induced surface potential at the instant immediately after charging ($t = 0$) is hard to attain experimentally, the initial measured potential $V_0$ is used instead of $V_1$. This introduces some error due to a discrepancy between these two quantities which depends on time needed for obtaining $V_1$. It is obvious that the measured data being used in (3.19) would result in variations of the right hand side of (3.19) due to the experimental errors.

As noted in section 3.4.3, the normalized decay rate obeys the power-law dependence:

$$-\frac{dV(t)}{V_0 dt} = \begin{cases} M_1 \cdot t^{-n_1} & t < t_T \\ M_2 \cdot t^{-n_2} & t > t_T \end{cases} \tag{3.20}$$

Polarization displacement current measured for the filled enamel (chapter 2) is illustrated in Figure 3.21. Recall that the experiments were carried out at room temperature and the applied voltage $V_2$ was 100 V. Also, the current component due to intrinsic conduction $\sigma$ has already been subtracted from the measured results. As seen, the current curve has two regions with different slopes close to –1. The knee point is observed at time $t_K \sim 10^3$ s, which is close to the characteristic time of the normalized decay rate d$V/V_0$d$t$ (see Figure 3.11). Hence, one writes for the curve in Figure 3.21:

$$i(t) = \begin{cases} B_1 \cdot t^{-a_1} & t < t_K \\ B_2 \cdot t^{-a_2} & t > t_K \end{cases} \tag{3.21}$$

Laplace transform of the power-law function $t^{-\alpha}$ ($\alpha$ is a positive value but not integer) can be expressed as

$$\mathbf{L}\left\{t^{-\alpha}\right\} = \frac{\Gamma(1-\alpha)}{p^{1-\alpha}} \tag{3.22}$$

where the gamma function is defined by

$$\Gamma(\alpha) = \int_0^\infty x^{\alpha-1} e^{-x} dx \tag{3.23}$$

Therefore, the right hand side of (3.19) becomes:

$$R = \frac{B_i \cdot M_i \cdot \Gamma(1-a_i) \cdot \Gamma(1-n_i)}{V_2 \cdot p^{2-(a_i+n_i)}} = \frac{E_i}{p^{e_i}} \tag{3.24}$$

Here, $B_i$, $M_i$, $a_i$, $n_i$ are defined in (3.20) and (3.21), $i$ = 1, 2.

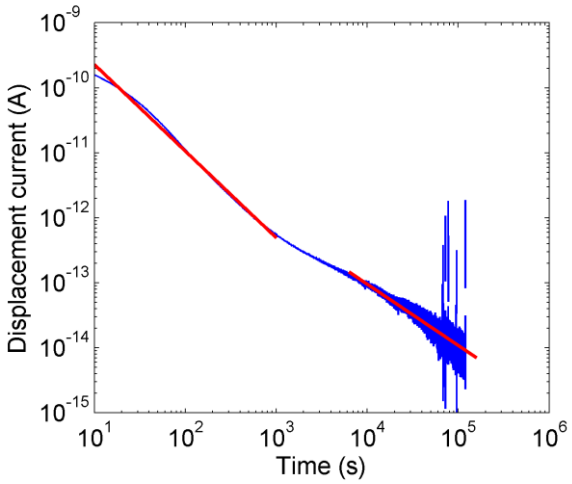


*Figure 3.21. Displacement current i(t) obtained at room temperature for the filled enamel. Straight lines are introduced for fitting the experimental results.*

Calculated results of the numerator $E$ and the exponent $e$ are illustrated in Figures 3.22 and 3.23 for the studied materials. Results are shown separately for two time intervals in either side of the knee point. Each experimental result is represented by a point in the coordinate system, in which the ordinate presents the ratio between the numerator $E$ and the geometric capacitance $C_0$ of the sample used in polarization current measurement, whereas the abscissa presents the exponent $e$. The horizontal dashed line corresponds to the equality $E = C_0$, and the vertical dashed line – the equality $e = 0$. The intersection of these dashed lines is marked by the point DP corresponding to both equalities $E = C_0$ and $e = 0$. In other words, the point DP shows the fulfilment of the experimental data to the relationship (3.19), meaning that surface potential decay is due to dipolar polarization. Note that the geometrical capacitance used in the polarization current measurement is 34 pF and 27 pF for the samples of the filled and the conventional enamels, respectively.

For the filled enamel, the experimental results obtained for instants longer than the characteristic time ($t > t_T$) are represented by points close to the point DP (indicated by the region limited by dotted line in Figure 3.22): the numerator $E$ varies within less than one order of magnitude around the geometric capacitance $C_0$ and the exponent $e$ is close to zero. This indicates that dipolar polarization may contribute effectively to the decay of surface potential during this period. For the time less than the characteristic time ($t < t_T$), the experimental results are illustrated by points that are far from the point DP: the exponent $e$ is larger than it is in the previous case, while the numerator $E$ is far below the value of the geometrical capacitance $C_0$, suggesting that other mechanism may be dominating. For the conventional enamel, similar verification suggests that dipolar polarization is not dominant in the decay process at either time duration (Figure 3.23). It should be noted that a more complicated mechanism may act in the conventional enamel due to the presence of two interfaces in its multilayered structure.

### 3.5.3 Charge injection

The relaxation and transport of charges in insulation with multilayered structure has not been fully understood yet. For single-layer insulation, on the contrary, various models based on charge injection and transport have been proposed to explain the experimental data on surface potential decay. One of these models is described here and used for analyzing the decay

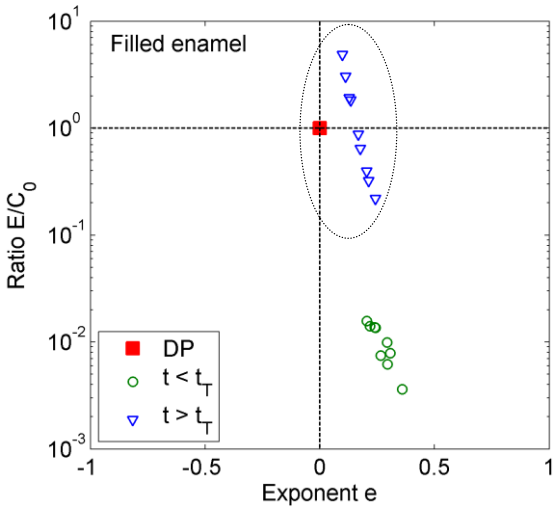


*Figure 3.22. Calculated results for the numerator E and the exponent e in (3.24) for the filled enamel.*

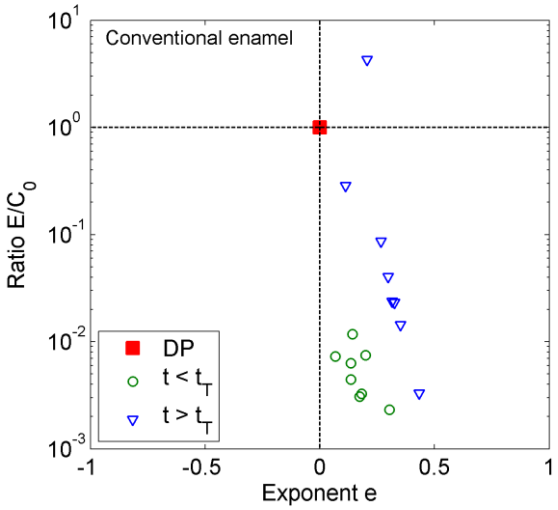


*Figure 3.23. Calculated results for the numerator E and the exponent e in (3.24) for the conventional enamel.*

process in PAI layer firstly. A hypothesis of surface potential decay for the multilayered insulation is discussed afterwards.

#### 3.5.3.1 Background

Von Berlepsch [37] has proposed a model making use of the concepts of instantaneous partial injection and hopping transport of charges between traps in the insulation bulk. Considering the positive polarity of the charging corona as an example, when positive ions are close to the insulation surface, hole-electron pairs are formed in the material bulk. While electrons may neutralize positive ions deposited, holes can transport further in the bulk in the field direction [53]. Dynamics of the created charges largely depends on the energy distribution of localized states in insulating materials. In general, surface traps are considered as deeper than bulk traps. Thus, a part of charge carriers is trapped in deep surface traps and will not be released within the measuring time, whereas the remaining part of charges can be injected in the bulk.

The bulk is characterized by both shallow and deep traps. The equilibrium of charge carriers in shallow localized states results in the transport with a shallow-trap-modulated mobility $\mu$, which is assumed to be field-dependent:

$$\mu = \mu_0 E^{n-1}(x,t) \qquad n \geq 1 \tag{3.25}$$

where $\mu_0$ is the low-field mobility, $n$ is the fixed exponent. In general, charge transport is characterized by a transit time $t_{tr}$ corresponding to the arrival of charges in the leading front at the grounded electrode. On the other hand, the deep bulk traps can capture charge carriers with a trapping rate $\omega$, associated with the life time of charges before being captured $\tau = \omega^{-1}$. Charges captured in traps can be then released back to transport with a certain release rate $r$.

The following analytical formula has been derived for describing the evolution of the surface potential with time for $t < t_{tr}$ [37]:

$$V(t) = V_0 - \frac{\mu_0}{n+1}\left(\frac{V_0}{d}\right)^{n+1}[1-(1-\rho_0)^{n+1}]\frac{1}{R}\left(rt + \frac{\omega}{R}\left(1-\mathrm{e}^{-Rt}\right)\right) \qquad t < t_{tr} \tag{3.26}$$

Here, $V_0$ is the initial surface potential, $d$ is the sample thickness, $\rho_0$ is the partial injection parameter ($0 < \rho_0 \leq 1$), $R = r + \omega$. The author [37] has highlighted the identity of the life time of charge carriers $\tau$ and the characteristic time $t_T$ corresponding to the knee point in the decay rate curves. In other work [38], the characteristic time $t_T$ is elucidated by the transit time $t_{tr}$. The mentioned model is successful in interpreting the cross-over phenomena observed in experimental results for several polymers such as HDPE.

#### 3.5.3.2 Surface potential decay mechanism for the PAI layer

The model proposed in [37] was utilized in the present study for fitting the measured surface potential decay characteristic for PAI layer provided in section 3.4.4. The results are shown in Figure 3.24 where very good agreement between theoretical and experimental data can be observed (the deviation is less than 0.18%). Parameters attained from the fitting are provided in Table 3.3. It should be noted that the obtained life time of charges before being captured by traps ($\tau \approx 40$ s) is lower than the characteristic time defined by experimental results ($t_T \approx 70$ s). Therefore, the parameters shown should be considered as intermediate results rather than final results. A model containing a system of transport equations provided in [37] should be developed for verifying them.

#### 3.5.3.3 Hypotheses of potential decay mechanisms on insulation coating of the enameled wires used

The analysis shows that the relation between the decay rate of surface potential and the displacement current of the filled enamel partially supports the decay model based on dipolar polarization. This implies the contribution of charge injection and transport to the decay process. The common feature for the charge injection is the presence of electric field as high as $10^7$-$10^8$ V/m in the insulation. In the present study, the initial field inside the samples varied in the range of $(2.8\text{-}6.8)\times 10^7$ V/m depending on the charging voltage magnitudes and the thickness of enamels used. Therefore, charge injection might take place being followed by the hopping transport of charges between traps within the insulation bulk. It is important to note that the role of interfaces between polymeric layers in the studied enamels cannot be ignored when considering the decay mechanism. As it is exhibited by the space charge measurements in the bulk of a two-layer insulation [54], the interface acts as a barrier

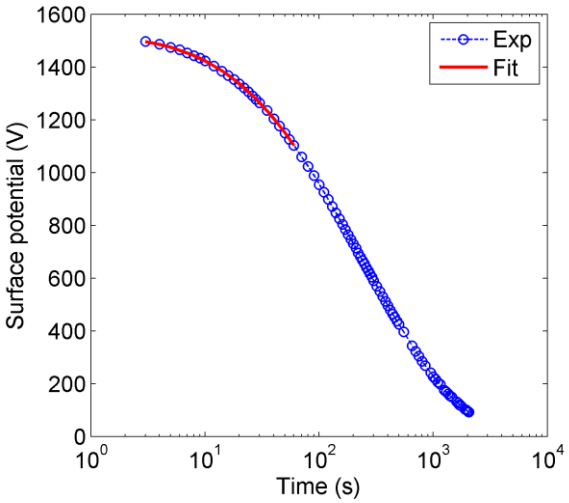


*Figure 3.24. Fitting experimental results of surface potential decay of PAI layer by the model developed in [37].*

*Table 3.3. Parameters obtained from fitting surface potential on PAI insulation by the model proposed in [37]*

| | |
|---|---|
| Low-field mobility $\mu_0$,($m^2V^{-1}s^{-1}$) | $3.90\times10^{-17}$ |
| Mobility of the leading front, $\mu_L$ ,($m^2V^{-1}s^{-1}$) | $2.73\times10^{-14}$ |
| Exponent of the field-dependent mobility $n$ | 1.3747 |
| Partial injection parameter $\rho_0$ | 0.3515 |
| Release rate $r$, $s^{-1}$ | $1.19\times10^{-2}$ |
| Mean capture time before release $1/r$, s | 84.3 |
| Trapping rate $\omega$, $s^{-1}$ | $2.53\times10^{-2}$ |
| Life time $\tau = 1/\omega$, s | 39.6 |
| Transit time $t_{tr}$, s | 35.3 |

hindering charge transport through the bulk insulation. Hence, the model based on charge injection and transport discussed above for the single layer insulation may not be suitable for analyzing the decay process in the multilayered insulation. Modifications should be introduced in the model to account for the effect of the interface(s).

Based on the provided analysis, one can suggest that the surface potential decay on the filled enamel is controlled by a combination of charge injection, hopping transport, and slow polarization. The charge injection and transport seem to be the dominating mechanisms during the first stage, starting immediately after corona charging up to the characteristic time. When charges reach the interface between two layers in the enamels, the charge transport becomes limited. This could be due to the existence of a high energy barrier that a majority of

charge carriers cannot overcome in order to be injected into the second layer. As a result, charges arrived at the interface would be mostly captured in the deep traps existing in the interfacial regions. A minor part of charge carriers able to inject into the bulk of the second layer continues the hopping transport until reaching the grounded copper wire. The effect of the interface can cause the rapid reduction of the potential decay rate observed after the knee point, see Figure 3.11. Meanwhile, the electric field created by charges at the sample surface and at the interface between layers may account for the molecular orientation as well as interfacial polarization in the insulation. The formation of bound charges modifies the electric field in the bulk that finally results in the decay of surface potential. While the effect of charge injection and transport in the total decay process weakens, the contribution of polarization relaxation processes gradually increases. As a support for the proposed hypothesis, the interfacial polarization between two insulation layers of the filled enamel has been characterized by a loss peak frequency as low as ~$10^{-5}$ Hz corresponding to a relaxation time of ~$10^4$ s (see chapter 2). Subsequently, as the polarization is stabilized, the potential decay is mainly due to intrinsic conduction. This can be attributed to the closeness of the calculated apparent bulk conductivity at the end of the decay process and the material conductivity obtained by the standard method (see Figure 3.19).

Another hypothesis for the decay mechanism of the filled enamel accounts for a contribution of the bipolar charge injection [55]. Under high electric field, charges can also be injected to the bulk from the metal-insulation interface between the conductor and the insulation. Here, charge injection appearing at the metal-insulation interface can be described by Schottky's law. The transport of charge carriers after injection is similar to that proposed in the previous hypothesis. The validation of suggested decay mechanisms should be proved experimentally, where the use of advanced measuring techniques such as pulsed electro-acoustic (PEA) [56] that allows for resolving space charge distribution in the bulk, is highly appropriate. Besides, computer modeling can also be an effective tool for this purpose.

A mechanism of surface potential decay similar to that described above may act in case of the conventional enamel. Charge injection is likely to take place in the initial stage after corona charging. The knee point was observed at the time of ~ ($3\times10^3$-$10^4$) s after which the contribution of polarization relaxation process dominate. However, polarization is still not the main reason for potential decay afterward, as shown in section 3.5.2. The presence of the two interfaces in the material structure may give rise to a more complex decay mechanism of surface potential. This topic, however, is out of the scope of the present study. Experimental investigations of charge distributions in the insulation bulk are required for elucidating the actual decay process.

### 3.5.4 Examining the decay mechanism for the sample surface

The normalized decay rate $dV/V_0dt$ obtained in section 3.4.3 demonstrates the integral effect of all mechanisms acting during the decay process. This quantity was always calculated for the sample center as the probe was kept at this location for continuously monitoring surface potential during the decay process. The normalized decay rate can also be calculated for other positions on winding surface by utilizing the decay of surface potential shown in Figure 3.8; however the obtained results may suffer from a large error as few data are available due to the limited number of scans. Thus, the decay mechanism for the sample center has been analyzed so far. The computer simulation provided in the present section aims at proving that the discussed mechanism of potential decay is also applicable for the surface area, at least where the charge injection is possible.

The decay of surface potential was modelled by solving equation (3.27) for the decay rate of the normalized surface potential in the simulation tool Comsol Multiphysics

$$-\frac{dV(t)}{V_0 dt} = \phi_E(t) \tag{3.27}$$

The measured surface potential distribution in the direction along wires and across the sample center was selected for comparing with the simulated results. Thus, the simulation was performed for the one-dimensional domain representing the gas-insulation interface. The function $\phi_E(t)$ taking into account the effect of all mechanisms acting during the decay process was obtained by fitting the curves for the decay rate measured at the sample centers shown in Figure 3.11. The surface potential distribution measured at 3 min after charging was set as the initial condition for the simulation since it is the first experimental data obtained for the selected direction.

An example of simulated results is shown in Figure 3.25 for the filled enamel charged by positive corona at 4 kV. The simulated results agree fairly well with the experimental data, especially for positions between 2 and 3 cm, i.e. the surface area around the sample center which has a diameter of 1 cm. Outside this region, the simulation shows a faster decay than the experiment. This could due to the field-dependence of charge injection [35, 37]. In the model, an identical normalized decay rate was used for the whole surface implying that a constant proportion of charges is injected into the bulk, regardless the level of the initial potential. In reality, the reduction of the initial surface potential when going from the center to peripheral area decreases the proportion of charges injected into the bulk [37], resulting in a slower decay process as exhibited in the measured results. Nevertheless, the developed simple model demonstrates that the discussed mechanism of surface potential decay is applied not only for the sample center, but also for other part on the surface.

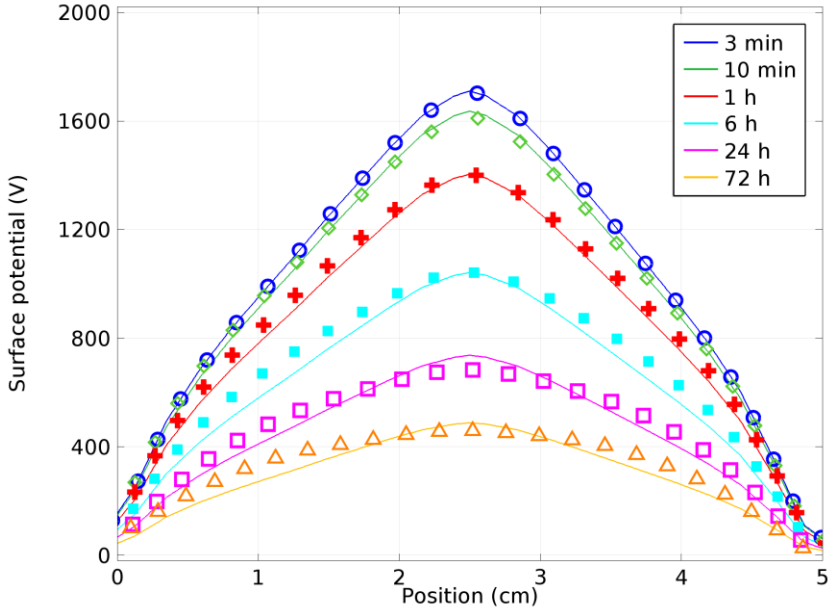


*Figure 3.25. Simulated results of surface potential for filled enamel charged by positive corona. The experimental results are provided by markers for comparison.*

In summary, the decay of surface potential of the filled enamel used in this study is likely governed by the injection of charges into the bulk at the initial stage immediately after corona charging and charge transport during the following ~$10^3$ s. The subsequent stage is dominated by dipolar polarization until ~$10^5$ s after charging due to the dielectric properties of the insulation. Thereafter, intrinsic conduction is responsible for the decay process, as the polarization becomes stabilized. Similar potential decay mechanism is also applied for the conventional enamel used, yet it seems to be more complicated due to the presence of two interfaces in its three-layer structure.

## 3.6 Material properties deduced from surface potential measurements

### 3.6.1 Trap density distribution

Assuming that a slow decay of surface potential is due to a long de-trapping time of charges from localized states in materials, one can employ a demarcation energy model [30, 32] for analyzing the decay process. Demarcation energy is the energy level below which all localized states are filled by the charges, and above which all localized states are emptied. The depth of traps $E_t$ or the gap between the mobility edge $E_0$ and the demarcation energy level $E_m$ is determined by the time duration that charges are captured by the traps as indicated in (3.1):

$$E_t = E_0 - E_m = kT \ln(\upsilon_0 t).$$

The attempt-to-escape frequency $v_0$ has been evaluated for polystyrene ($v_0 \sim 10^{11}$ s$^{-1}$) [32]. On the other hand, it is accepted that $v_0 \sim 4\times 10^{13}$ s$^{-1}$ for low density polyethylene and polypropylene [57]. In this study, we assume that $v_0 \sim 10^{12}$ s$^{-1}$. The trap density at a certain energy level $E_t$ can be expressed by a quantity proportional to $t$d$V$/d$t$ [57]:

$$N(E_t) = \frac{\varepsilon_0 \varepsilon_t}{kTf_0(\mathrm{E}_t)\delta dq}\frac{tdV}{dt} \tag{3.28}$$

Here $f_0(E_t)$ is the rate of initial occupancy of traps ($f_0$ = 1/2), $\delta$ is the thickness of injected charge layer, $d$ is the sample thickness, $q$ is the elementary charge. The distribution of hole traps can be found in case of positive charging voltage, whereas the distribution of electron traps is obtained by applying negative charging voltage.

Examples of the trap density distributions obtained for the studied materials are shown in Figure 3.26. As seen, the profiles show field-dependent behavior and the trap density increases rapidly with the charging level. This could be attributed to the increased amount of charges injected in the insulation bulk with increasing charging voltage magnitude. For the conventional enamel, the trap depth corresponding to the maximum density remains practically unchanged with increasing charging level. On the other hand, this observation is only applicable for two charging voltages (4 kV and 4.5 kV) for the filled enamel, whereas the characteristic corresponding to 3.5 kV is shifted towards higher energies.

The density distribution of electron and hole traps for both enamel insulations are compared in Figure 3.27. One may observe that the trap distributions in the conventional enamel are similar for both the hole and the electron traps and they are characterized by a peak at ~1.03 eV. On the other hand, for filled enamel the trap distributions are shifted towards lower energy level and the peaks are observed at 0.97 and 1.0 eV for the hole and the electron traps,

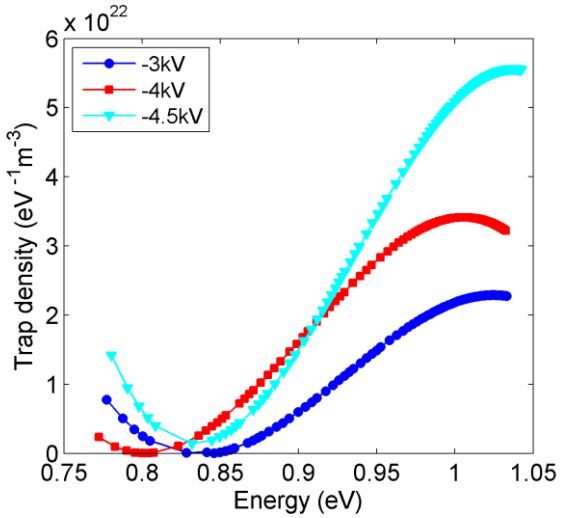


*a) Electron traps, conventional enamel*

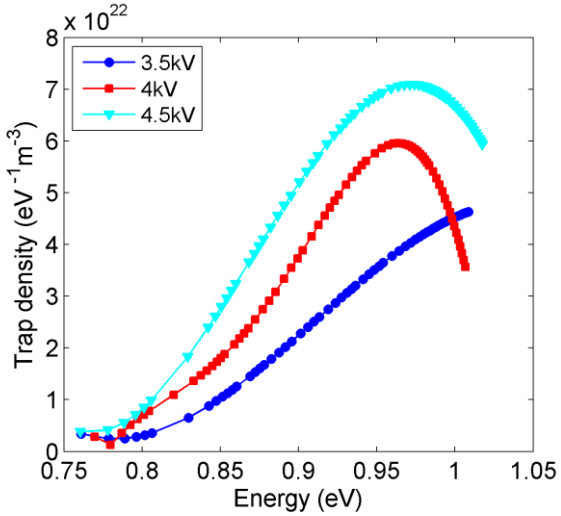


*b) Hole traps, filled enamel*

*Figure 3.26. Trap density distributions of enamels derived from surface potential measurements. Charging level is indicated in the legend.*

respectively. In addition, trap density is higher for the filled enamel than for the conventional one. Accordingly, the addition of chromium oxide filler gives rise to shallow traps, probably appearing in the interfacial regions between the fillers and the polymeric insulation, thus mitigating the hopping transport of charges in the filled insulation.

It has been noted in [29] that the obtained trap distribution does not have physical meaning if the potential decay process is solely governed by dipolar polarization mechanism, where the density of free surface charges is constant and the potential decay is due to the interaction of bound charges created in the insulation bulk and the free charges deposited on insulation surface. However, as analyzed in the previous section, it is not the case here.

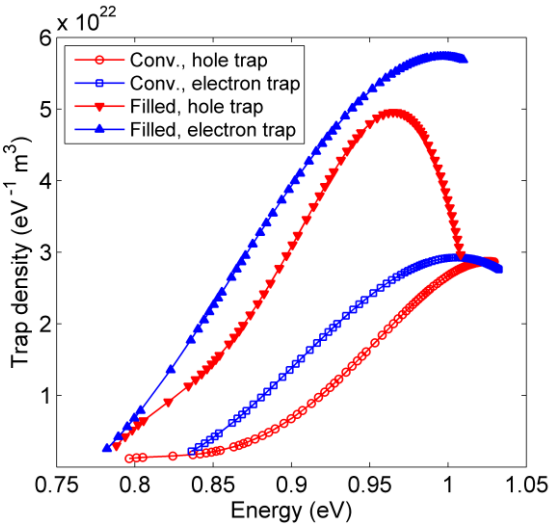


*Figure 3.27. Trap density distributions of conventional and filled enamels derived from surface potential measurements at charging level of 4 kV.*

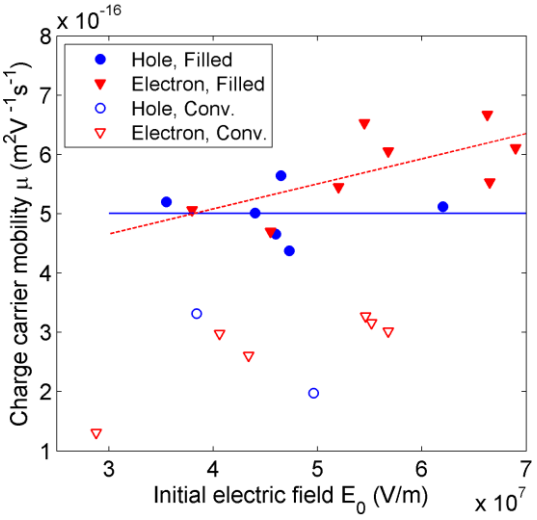


*Figure 3.28. Charge carrier mobility as functions of the initial electric field. The lines indicate tendensies of the variations.*

### 3.6.2 Charge carrier mobility

Charge carrier mobility $\mu$ can be evaluated from results of surface potential decay measurements using the approach presented in [36] where the following expression was suggested:

$$-\left(\frac{dV}{dt}\right)_{t=0} = \frac{\mu}{2}\left(\frac{V}{d}\right)^2_{t=0} \tag{3.29}$$

Here, $V$ is surface potential, $d$ is the sample thickness, and the left hand side represents the initial decay rate. The experimental data for positive and negative charging provide the drift mobility of holes and electrons, respectively. The calculated charge carrier mobilities are shown in Figure 3.28 as functions of the initial electric field. As can be seen, the mobility of

both charge carriers is higher for the filled enamel than for the conventional one. For both enamels, the electron mobility tends to increase with enhancing initial electric field. On the other hand, the mobility of holes does not show field-independent behavior. Particularly in case of the conventional enamel, any dependence is hard to establish due to the fact that only few data points were obtained.

The calculated charge carrier mobility is in the order of $10^{-16}$ $m^2V^{-1}s^{-1}$. The obtained values can hardly be verified because experimental data on mobilities of charge carriers in enamel insulation are not available in the literature. Therefore, an experimental study needs to done, e.g., by utilizing the time-of-flight method [58].

## 3.7 Summary

Surface potential measurements were conducted for characterizing the electrical properties of the enamel insulations. Experiments were performed for the winding samples of enameled wires as well as for the flat samples of PAI resins with and without filler. Experimental results show that the potential decay is mainly due to bulk mechanisms rather than due to surface leakage and/or gas neutralization. The main processes contributing to surface potential decay on the enamel insulations are charge injection, slow polarization and intrinsic conduction. For the filled enamel coating used, charge injection and transport took place on early stages (just after charging), followed by slow polarization process which dominate at intermediate times, and, finally, intrinsic conduction became crucial at long instants. The involvement of slow polarization might be due to the presence of the interface in the insulation structure that hinders the charge transport through the bulk. For the conventional enamel used in the present study, a more complicated decay mechanism may act as two interfaces are present.

Furthermore, the distribution of trap density was derived, showing the increase of shallow traps brought about by the introduction of chromium oxide into enamel insulation. The charge carrier mobility was similar for both hole and electron for the considered materials and a weak field-dependent behavior was observed.

# 4 Partial discharge characterization at fast rising voltages

## 4.1 Literature review

This section provides an overview of ongoing studies on PD measurements and analyses in enamel insulations exposed to fast rising voltages. First, a background concerning the impact of distorted voltages on motor insulation is presented. The next section analyzes results of investigations on the PD activity in enamel insulations. The final section focuses on the development of PD-resistant enamel insulation.

### 4.1.1 Increased stresses in insulation systems exposed to distorted voltages

#### 4.1.1.1 Enhanced electrical stress

Windings of electrical motors are made of enamel insulated wires. Typically, the impedance of a motor winding is much higher than that of connecting cables and, hence, voltage reflection during propagation between voltage source and the motor is unavoidable. This may result in voltage overshoot in the waveform front transmitted to motor terminals. The maximum value of voltage overshoot is determined by the length of a connecting cable and the rise time of the applied voltage. Particularly, the combination of a short rise time and a long cable may lead to unacceptable overvoltage on motor insulation [59, 60]. Thus, due to a high rate of voltage rise, first turns of motor windings experience a major part of voltage drop on the entire winding [61]. Additionally, voltage distribution is extremely uneven along the winding due to different values of turn-to-turn and turn-to-ground capacitances of winding insulation [61]. Furthermore, it is noteworthy that in motor windings, the first turns are adjacent to the last ones, and hence, the insulation between these turns is exposed to a significantly increased electrical stress. As an example, for low power motor with random-wound windings, the voltage drop on the first turns may amount up to 90% of a maximum voltage on the insulation of entire winding at a rise time of 50 ns [62]. Such strong electric stress on turn-to-turn insulation gives rise to PD activity, which aggravates the thermal stress in the insulation. Finally, it can lead to a premature breakdown of the winding insulation.

#### 4.1.1.2 Enhanced thermal stress

The thermal stress on insulation systems due to distorted voltage shapes has been a subject of several investigations, see for example [63-65]. When a sinusoidal voltage is applied to a conductor, a capacitive current appears in the insulation, resulting in the dielectric loss

$$P(\omega) = \omega C(\omega) \tan\delta(\omega) U^2 \tag{4.1}$$

where $\omega$ being the angular frequency, $C(\omega)$ is the capacitance, $\tan\delta(\omega)$ is the loss factor and $U$ is the rms value of the applied voltage.

In reality, the insulation system may be exposed to a non-sinusoidal voltage that can be presented as the sum of a number of sinusoidal components (harmonics) at different frequencies. Therefore, the total dielectric loss will be [64]:

$$P = \sum_{n=1}^{\infty} n\omega_0 C(n\omega_0) \tan\delta(n\omega_0) U_n^2 \tag{4.2}$$

where $\omega_0$ is the angular frequency of the fundamental component, and $U_n$ is the rms voltage of $n^{th}$ harmonic at frequency $n\omega_0$.

If the capacitance $C(n\omega_0)$ and the loss factor $\tan\delta(n\omega_0)$ are independent on frequency, the dielectric loss is directly proportional to the sum of frequencies. High frequency components are usually at relatively lower amplitude as compared to that of the fundamental component, but they produce dielectric losses in several times higher than that of the latter. For polyethylene terephthalate (PET) and epoxy resin that are usually used in motor insulation, the rate of rise of the loss factor $\tan\delta(\omega)$ with increasing frequency is higher than the rate of reduction of the capacitance $C(\omega)$ [64]. Consequently, the product of the capacitance and the loss factor will rise with frequency and the dielectric loss will be enhanced. In particular, the power loss of PET under semi-square waveform with a voltage rise time of 50 µs is 4-8 times higher than that under power frequency voltage with the same amplitude [64]. High dielectric losses increase the surface temperature of motor insulation and the higher frequency and the shorter rise time make the surface temperature of electrical motor higher [63]. The resulting thermal stress accelerates insulation degradation, especially being combined with PD activity.

### 4.1.2 PD activity

The enhanced electrical and thermal stresses lead to strengthening of PD activity in motor insulation systems. In turn, PDs in air gaps between enameled wires heat and radiate the insulation as well as create mechanical and chemical energies that erode the insulation [66]. The erosion on insulation surface due to PD activity can be analyzed by using images obtained from Scanning Electron Microscopy (SEM). The method has been used e.g in [4] and showed different erosion patterns for conventional enamel and PD-resistant enamels that reveal the role of fillers in PD resistance of materials.

The effect of distorted voltages on enamel insulations have been investigated utilizing several voltage waveforms: sinusoidal voltages, square-like voltages (both unipolar and bipolar), and PWM voltages; all of them are at frequencies higher than the power frequency. It has been shown that PD behavior is strongly affected by the voltage waveform [2]. For sinusoidal and bipolar square-like voltages, PDs at low amplitudes appeared frequently at the rise front, whereas fewer PDs occured but at higher amplitudes in case of unipolar square-like voltage. Another observation was that the peak-to-ground value of PDIV under square-like voltage was two times higher for the unipolar than for the bipolar waveforms. Hence, the peak-to-peak value of the applied voltage has been suggested as the most influential factor affecting PD activity [2]. In recent work [67], the presence of voltage overshoot in the applied waveforms was considered, and thus, the PD patterns and insulation life times were compared for the sinusoidal, square-like, triangular, PWM voltages, as well as PWM voltage with superimposed overshoot. Thus, the shortest insulation life time has been found for the last applied waveform.

PD extinction voltage (PDEV) has been considered as the governing parameter once PDs appear in the insulation systems. A method for accurately determining PDEV has been introduced in [68]. For several test objects, PDEVs were strongly affected by voltage rise times. In case of twisted pairs of enameled wires exposed to square-like voltage, PDEV was found to be 25% lower for the voltage with 2 µs rise time as compared to that of 100 µs rise time [68].

Numerous works [1, 2, 69] have reported the influence of high frequency harmonics and short voltage rise times on insulation life time. For example, aging tests have been conducted by using square-like voltages at a frequency range from 60 Hz to 20 kHz and rise times of 40-100 ns [69]. It has been noted that the number of cycles to breakdown (the product of time to breakdown and the pulse frequency) was constant for frequency lower than 5 kHz and decreased for frequency higher than 5 kHz. Consequently, the failure time was inversely proportional to the frequency below 5 kHz, whereas it was inversely proportional to the square of frequency above 5 kHz. In other words, insulation life time decreased dramatically with frequency. Similar results have also been obtained in [1], where the insulation failure time at 10 kHz was in several orders of magnitude lower than the corresponding time at 50 Hz. Additionally, insulation life time was generally decreasing with reducing voltage rise time.

It is worthwhile to notice the contribution of space charge accumulation due to PD activity in accelerating insulation degradation. Two types of space charges exist in enamel insulation, namely interfacial charges accumulated on insulation surfaces and trapped charges inside insulation bulk [2]. The amount of space charges accumulated is strongly affected by the frequency of applied voltage, i.e. higher frequency corresponds to lower charge density. The reason for this is a quick variation in electrical field preventing charges from penetrating inside insulation and, thus, charges remained on insulation surface may recombine with charge carriers of opposite polarity arising after voltage inversion. The impacts of interfacial charges and trapped charges on PD activity are different. The interfacial charge may decrease the electrical field in the air gap of a twisted pair, thus increasing PDIV. Meanwhile, charges trapped inside the insulation bulk enhance the electrical field, thus reducing PDIV. Furthermore, space charges also give rise to PD amplitude. As the applied frequency increases, charges created by PDs cannot leave the interface before polarity reversal. The residual charges intensify electrical field in the air gap, thereby increasing PD amplitude. This was illustrated by the increase of PD amplitude with frequency up to 500 Hz [2]. In contrast, the effect of space charges on PD amplitude was not observed for frequencies from 500 Hz to 10 kHz [2], which might be due to the fact that the space charges built up could not keep up with the high rate of polarity reversal.

In addition, lower PD amplitudes have been recorded for materials with higher surface conductivity [2]. This property has been explained by a dissipation of surface charges accumulated due to PD activity. Higher surface conductivity resulted in larger surface leakage current that reduced the residual surface charges and thereby the electric field in the air gap affecting the PD amplitude.

### 4.1.3 PD-resistant enamel insulations

Various measures have been proposed for avoiding the detrimental impact of distorted voltages on insulations of rotating machines. These include reinforcing insulation of first turns of the windings; impregnating wire insulation with resin or varnish for increasing PD inception voltage and restricting PD activity [66]; creating cables that can dissipate high frequency energy for connecting PWM inverters and motors [70]; developing PD-resistant materials [4-6, 27, 71]. Among the above mentioned methods, the PD-resistant insulation seems to be the most effective method for low-voltage induction motors.

The use of several inorganic micro-particles in the outer layer of two-layer enamel insulations has been considered [27]. Among the fillers used, $Fe_3O_4$ and talc additives resulted in the most considerable increase in insulation life time, as well as the reduction in PDIV and PDEV. The result was attributed to the increase in electric conductivity of the filled

insulation. The simulation revealed that the increase in enamel conductivity gave rise to electric field in the space close to both wires, which lowered PDIV and PDEV. On the other hand, according to the experimental results, the PD repetition rate remained constant, while the discharge magnitude reduced. This decreased the total energy produced by PD activity, consequently lengthening insulation life time.

Recently, nanocomposite insulating materials were proposed for enameled wires, which brought about even more fascinating results [4, 5, 71]. Aging tests at severe voltage stresses in combination with thermal stress were commonly conducted. The results showed that increasing the nanofiller contents up to 10 wt% exponentially lengthened the time to breakdown up to several hundred times as compared to that of conventional insulation. There are, however, challenges in producing such materials. Thus, the shearing force in the kneading process must be high in order to evenly disperse nanofillers in insulation. In addition, there exists a threshold of filler content, over which the flexibility of developed materials decreases, thus weakening the electrical and mechanical properties [5].

Numerous hypotheses have been proposed, e.g. [4, 71], for explaining the improvement in PD performance of the filled enamel insulation. Most of the theories suggest the role of fillers in suppressing insulation erosion. Charges created by PD activity seem to focus on the organic polymeric base materials, while tend to avoid collisions with the inorganic fillers. Thus, the creeping distance (path of charge carriers) is lengthened and the energy produced during the erosion is reduced. This erosion mechanism is supported by the obtained SEM images. As the filler size decreases, the homogenous dispersion of fillers is more easily achievable and an improvement in PD performance may be more pronounced. Therefore, noticeable PD resistance is usually anticipated for nanocomposites rather than for microcomposites.

## 4.2 Experiments

This chapter presents a comparative analysis on PD behavior under PWM voltages with different rise times for the conventional and the filled enamels.

As for the test objects, twisted pairs of enameled wires were prepared following the IEC 60851-5 standard [72]. The twisted pairs were connected to a voltage supply as illustrated in Figure 4.1. A bipolar PWM voltage (carrier frequency of 1 kHz, modulation frequency of 50 Hz, duty cycle of 34%) was utilized in the experiments. The applied voltage was adapted to different rise times by introducing a smoothness filter, whose component parameters are provided in Table 4.1. The ratio between the rise times of the applied voltage and the sinusoidal voltage at power frequency was used as a measure of the filtering level as introduced in [73]:

$$s = T_{r\_applied} / T_{r\_\sin}. \tag{4.3}$$

The first step of each test was to determine a PDIV level. Subsequently, the PD measurements were performed at two voltage levels (2.5 and 3.5 $kV_{pp}$), which well exceeded the magnitude of PDIV. The peak-to-peak value of the applied voltage was used as it was the governing factor of PD activity [2]. Note that there was a challenge of detecting PDs at fast rising voltages such as PWM waveform, as the high frequency content of the PWM voltage is difficult to distinguish from a PD signal. This challenge was overcome by using the time domain technique that was recently introduced in [68, 73]. For this, a PD decoupler was connected to point A of the test circuit (Figure 4.1). The PD signal was amplified by resonances due to impedance mismatch at the terminal of a coaxial cable. Since PDs have a

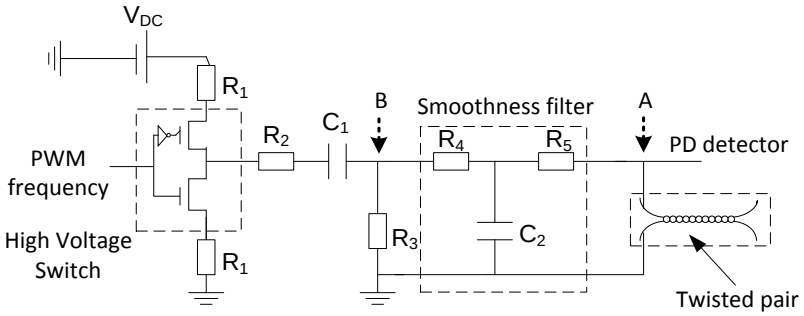


*Figure 4.1. Experimental setup.*

*Table 4.1. Parameters of filter components and corresponding characteristics of the applied voltage*

| Level | $R_4$, kΩ | $R_5$, kΩ | $C_2$, pF | $T_r$, µs | Smoothness |
|---|---|---|---|---|---|
| 1 | 0 | - | - | 1.1 | 0.0002 |
| 2 | 200 | 100 | - | 70 | 0.0119 |
| 3 | 2300 | 100 | 100 | 1000 | 0.170 |

stochastic nature whereas the applied voltage is more stable, the latter could be subtracted from the acquired signal, providing random signal of PD activity. Experimental data from 200 cycles were stored by means of a data acquisition card with sampling rate of 100 MS/s. Finally, PDEV was noted to accomplish each test. The experiment was repeated two times for each type of enameled wires at a specific voltage amplitude and rise time. Good reproducibility was observed in the measurements. More detailed information on PD analysis and the measuring system can be found in [73].

## 4.3 Preliminary results

The results of the measurements show that the PD inception and extinction voltages (Figure 4.2) were lower in case of filled enamel that can be considered as the effect of the filler. The addition of highly dispersive chromium oxide (relative permittivity $\varepsilon \sim 30$ at 1 kHz) into the base insulating polymer ($\varepsilon \sim 3.6$ at 1 kHz) provides an enhanced electric field localized on wire surfaces close to fillers particles. The critical electric field for PD inception is therefore more easily achievable for the filled insulation, thus resulting in lower PDIV level. On the contrary, such an enhanced electric field does not appear in the twisted pair of the conventional enameled wire, thus higher PDIV level can be observed.

The measured PD patterns are shown in Figures 4.3 and 4.4 for both insulation systems for two voltage rise times. As seen, at the rise time of 1.1 µs, PDs mainly occurred at each voltage flank (Figure 4.3), where the voltage steepness d$V$/d$t$ was as high as 2-3 kV/µs. PDs with high amplitudes (above 8 V) accounted for approximately half of the total PD number in case of conventional enamel, whereas a few PDs at similar amplitudes were recorded for the filled material. This suggests lower average PD amplitude for the filled enamel. It should be noted that the PD pattern does not alter significantly when the rise time was increased from 1.1 to 70 µs, therefore the latter is not shown here. Further, the applied voltage with the rise

time of 1000 µs can be considered as a superposition of a sinusoidal waveform at power frequency (50 Hz) and a triangular component at frequency close to the carrier frequency (1 kHz). As a result, the PD pattern is governed by the high frequency component characterized by high voltage steepness. Accordingly, PDs with amplitude as high as 10 V still appeared in this case as seen in Figure 4.4, but less frequently as compared to the case of voltage rise time of 1.1 µs. In addition, a majority of PDs at high voltage smoothness are of low amplitude (below 0.5 V), which may be less damageable for the insulation surface compared to PDs with high amplitude appearing at low smoothness level.

An analysis on the PD characteristics was conducted, in which the average PD amplitude and number of PDs per cycle were determined and compared for the investigated materials. As seen in Figure 4.5, the average PD amplitudes were 2-3 times higher for the conventional enamel than for the filled one at the voltage rise time of 1.1 µs. At the same time, the numbers of PDs per cycle were at the same level. The average PD amplitudes were substantially diminished at two longer voltage rise times and were similar for both enamels indicating that

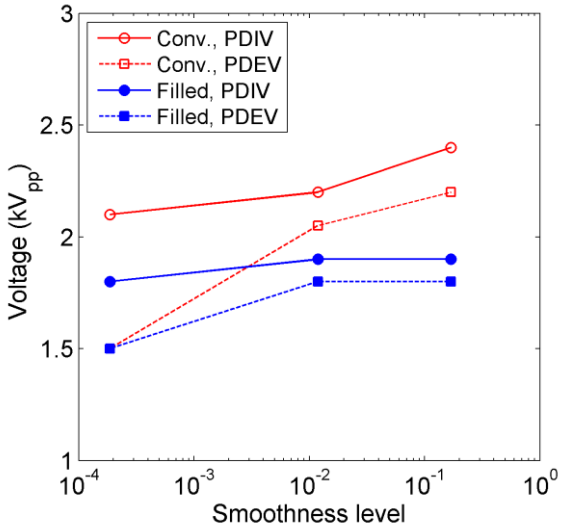


*Figure 4.2. PD inception and extinction voltages for both enamels.*

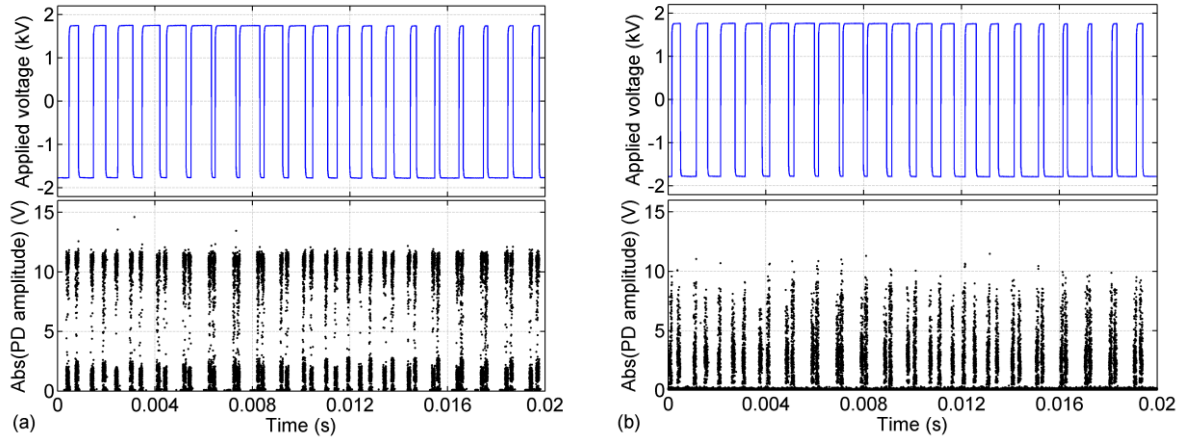


*Figure 4.3. PD patterns obtained for conventional (a) and for filled enamels (b) under PWM voltage of 3.5 $kV_{pp}$ at rise times of 1.1 µs.*

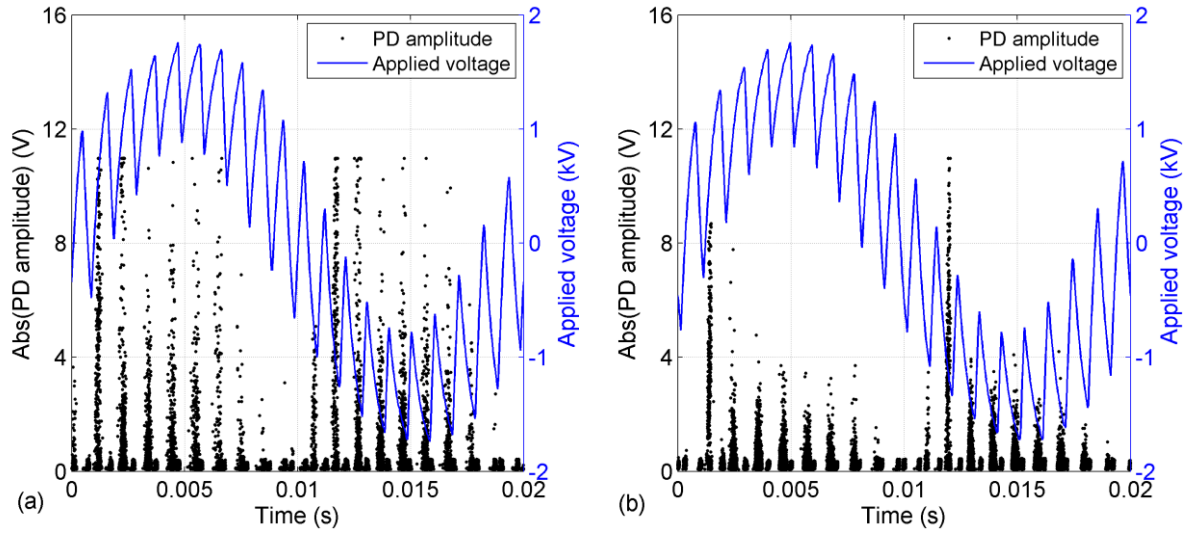


*Figure 4.4. PD patterns obtained for conventional (a) and for filled enamels (b) under PWM voltage of 3.5 $kV_{pp}$ at rise times of 1000 µs.*

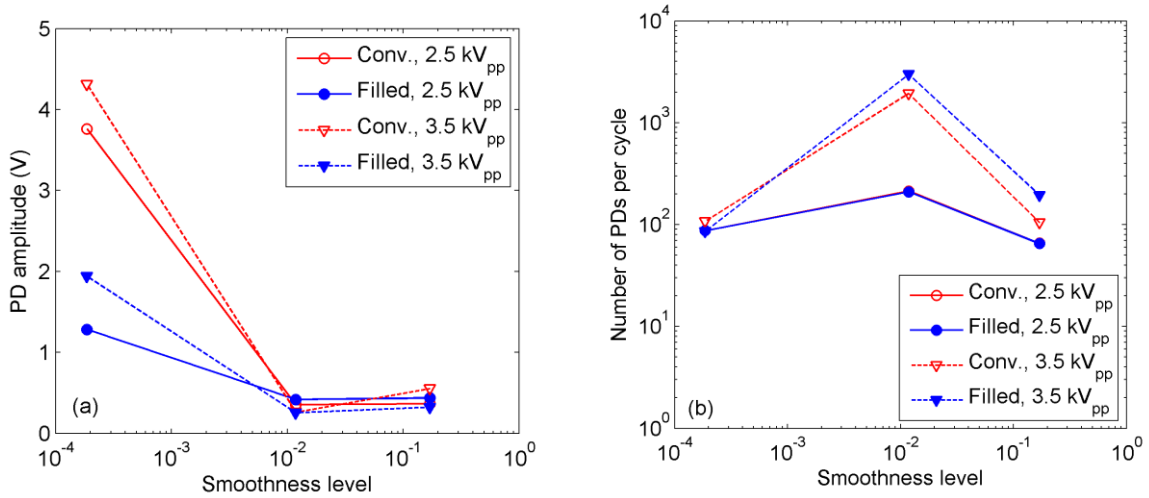


*Figure 4.5. Average PD amplitude (a) and number of PDs per cycle (b) for both enamel insulations when exposured to PWM voltage at different smoothness levels (note corresponding voltage rise times in Table 4.1).*

PD amplitude might become stabilized after the applied voltage has reached a certain smoothness level. It can be noticed from the figure that the addition of chromium oxide does not change the number of PDs per cycle at the applied voltage of 2.5 $kV_{pp}$. However, it tended to increase their number and to lower the PD amplitude at 3.5 $kV_{pp}$. In addition, the dependence of the number of PDs per cycle on smoothness level is characterized by a pronounced maximum, similarly to the case of PDs in cavities reported in [73], where the maximum was achieved at smoothness level of ~0.002.

To characterize the PD resistance of insulating materials, measures of erosion depth have been commonly employed [4, 26]. The erosion is presumably caused by the cumulative effect

of large PDs as the energy produced by them may be sufficient to destroy insulation surface. Consequently, the impact of large PDs cannot be ignored even if only few of them occur. In the present study, "large PDs" are classified as those having amplitudes exceeding 1 V, which is 2-3 times higher than the average PD amplitude at voltage rise times above 70 µs. The properties of "large PDs" observed in this study are illustrated in Figure 4.6 for both enamels at different voltage rise times. As seen, a majority of PDs occurred at the shortest rise time of 1.1 µs can be considered as larger PDs, whereas only 3-10% of PDs at the other two rise times belonged to the same category. At the applied voltage of 2.5 $kV_{pp}$, the number of large PDs reduced with increasing voltage rise time (smoothness level in the figure). However, for the applied voltage of 3.5 $kV_{pp}$, a maximum is observed at the rise time of 70 µs. Although the number of large PDs was high in this particular case, their average amplitude was smaller (e.g. 2.5 V at 70 µs versus 6.5 V at 1.1 µs for the conventional enamel), thus lowering the total PD exposure at this rise time. These observations emphasize the influence of high voltage steepness in PD characteristics. It is important to note that the parameters of large PDs are not strongly distinguishable for the two enamel insulations, apart from the shortest rise time. In other words, the improvement in PD characteristics of the filled enamel became less noticeable when enameled wires were exposed to the filtered PWM voltages.

The observed PD characteristics can be elucidated by considering the development of PDs in a twisted pair. Starting with positive polarity as an example, increasing voltage magnitude gives rise to the electric field in air gap between the wires until it reaches a critical value at which PDs may occur. The corresponding applied voltage level is defined as PDIV. As the applied voltage exceeding PDIV, more PDs gradually occur. Discharges appearing in the air gap between two wires of the twisted pair result in charge deposition on insulation surfaces as shown in Figure 4.7a. Part of the deposited charges will remain on the surfaces even though charges decay due to an injection into the bulk or a transport along wire surface. The electric field created by the surface charges has an opposite direction as compared to that of the external field, thus leading to a reduction of the total field magnitude (Figure 4.7a). When the applied voltage changes its polarity, the surface charges may still remain. The electric field induced by the charges has the same direction as the external field, thus magnifying the total field in the air gap (Figure 4.7b). Therefore, PD characteristics will be affected by existing layers of surface charges as well as by their relaxation and decay. As it has been shown in chapter 2, the addition of highly conductive chromium oxide to enamel insulation has considerably accelerated the decay of charges deposited on insulation surface. Thus, charges created by PD activity on wire surfaces of the two enamels should have different relaxation times. In particular, more charges can remain on the surface of the conventional enameled wire than on the surface of the filled enameled wire. Due to this, the PD activity in twisted pair at different voltage rise times can be affected differently.

At the voltage rise time of 1.1 µs, the polarity reversal causes an extremely rapid increase of the total electric field in air gap between two wires that leads to the appearance of PDs with large amplitudes along the voltage flank. As the polarity reversal happens after ~1 ms, large amount of charge may still remain on wire surfaces. Since more charges remain on the conventional enamel, the PD amplitude is higher for this material than for the filled one. For the voltage rise times longer than 70 µs, the magnification of the total electric field in the air gap after polarity reversal would happen more slowly than in the previous case and, therefore, fewer PDs with high amplitude occur and the average PD amplitude is reduced.

The influence of interfacial charges on PD activity in twisted pairs requires further investigations. In particular, the clear understanding concerning mechanisms of charge relaxation and decay on enamel surfaces is important. In [2], a correlation between the

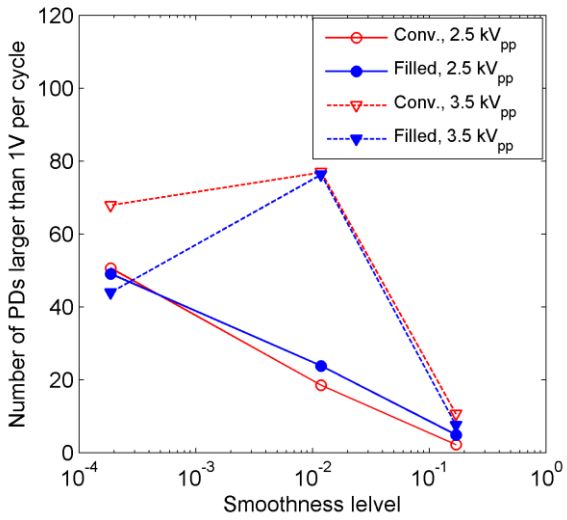


*Figure 4.6. Number of PDs larger than 1 V per cycle for both enamel insulations exposured to PWM voltages at different smoothness levels (corresponding voltage rise times are provided in Table 4.1).*

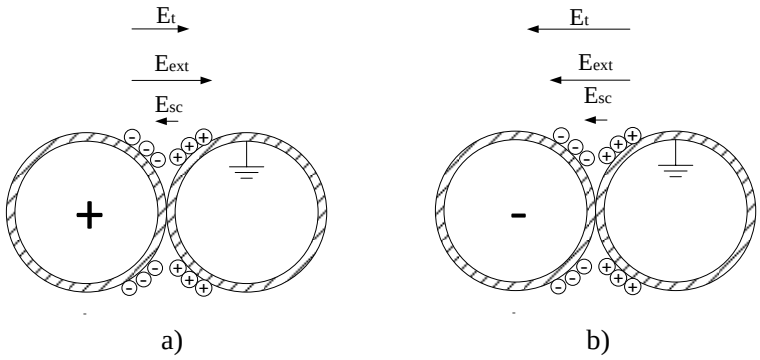


*Figure 4.7. Schematic representation of charge deposition on wire surfaces of a twisted pair due to PDs at positive polarity (a) and after polarity reversal (b). Here, $E_{sc}$, $E_{ext}$, and $E_t$ denote the electric field due to surface charges, the external, and total electric fields, respectively.*

reduced PD amplitude and relatively high surface conductivity of the enamel insulation has been discussed. This indicates the role of surface charge leakage in the decay process. However as shown in chapter 3 for the enamels used in the present experiments, the decay of charges deposited on wire surfaces is mainly due to the bulk neutralization rather than due to surface leakage.

## 4.4 Summary

PD activity was investigated for the conventional and $Cr_2O_3$-filled enamels exposed to PWM voltage with different rise times. The inception and extinction voltages, average amplitudes and numbers per cycle were utilized as PD characteristics. The rise time of PWM voltage was found to be the most influential factor affecting PD performance of the enamel insulations.

The average PD amplitudes were extremely high at the rise time of 1.1 µs and they were significantly reduced when the rise time exceeded 70 µs. Furthermore, a majority of PDs appearing at the shortest voltage rise time could be considered as being capable to erode insulation surface, whereas only a minor part of PDs at longer rise times might be damageable. The addition of chromium oxide filler to conventional enamel insulation provided lower PD inception and extinction voltages. It also decreased PD amplitude at the shortest voltage rise time while the effect was not observed at longer rise times. This property is presumably related to the decay of charges on wire surface. Experimental study should be further conducted to properly elucidate the role of the filler in PD activity of enamel insulations.

# 5 Conclusions

## 5.1 Dielectric properties

Dielectric properties have been measured for the PD-resistant enamel filled with chromium oxide and the conventional insulation. The conventional enamel used in the present study as the reference consisted of a PEI base coat, a PAI overcoat and a modified aromatic PA bonding coat. It is characterized by a dc volume conductivity as low as $6\times10^{-17}$ S/m. The measured dc volume conductivity of the PAI layer was ~$10^{-15}$ S/m, whereas the property of the other two materials was unknown. One may expect that PA layer is relatively more conductive than the PEI and PAI layers, whereas PEI is the most resistive material having dc conductivity at the same order as for conventional enamel coating. On the other hand, the chromium oxide filler is much more conductive than the polymeric insulation. The introduction of chromium oxide into the base polymeric material marginally increased the dc conductivity of the filled enamel as the modification was only in the PAI top layer and the percolation level has not been reached.

The use of the master curves allowed for analyzing the contribution of polarization relaxation processes in the investigated materials. The complex dielectric susceptibility of the conventional enamel was found to be primarily governed by interfacial polarization at low frequencies (~$10^{-6}$ Hz) and dipolar relaxation at high frequencies (~$10^{5}$ Hz). Chromium oxide is a strongly dispersive material, its dielectric response is dominated by the low frequency dispersion. Hence, the additive gave rise to both the real and imaginary parts of the complex permittivity of the filled enamel as compared to those of the conventional one. Further, the presence of chromium oxide fillers in enamel insulation resulted in the increase of low frequency dispersion as well as the appearance of interfacial polarization at their interfaces with the base polymeric material. Note that for both the studied materials, measurements were conducted in a wide range of temperature, showing the increase of dc conductivity and dielectric loss and the decrease of the real part of relative permittivity with temperature.

## 5.2 Surface potential decay measurements

Surface potential decay measurements were performed with the primary aim of characterization of material properties for the used enamel insulations. The decay process was found to be considerably accelerated for the filled enamel as compared to that for the conventional one. For both the considered materials, charge transport through the bulk was the dominant way of charge decay, whereas surface charge leakage and charge neutralization by gas ions were found to be insignificant. The potential decay behavior was initially attributed to the distinctive dc conductivity of the materials. The conduction model was utilized for characterizing the decay process, and the apparent bulk conductivity was derived. The strong field-dependent behavior was found for the bulk conductivity which could be due to non-linear mechanisms such as Poole-Frenkel or space charge limited current.

A detailed analysis revealed that not only intrinsic conduction but also charge injection and transport as well as dipolar polarization contributed to the surface potential decay of the filled enamel. Charge injection and transport were likely dominated at the initial stage (right after charging). Once mobile charges reach the interface between the base and the top coats, charge transport might be hindered due to the presence of deep localized states existing at the interface. At the same time, the presence of high electric field in the material activated the polarization relaxation processes, and their contribution to the potential decay gradually increased. Polarization was shown as the main factor contributing to potential decay in the subsequent stage (at $10^3$-$10^5$ s after charging). Finally, intrinsic conduction became prevalent in the decay process. The decay mechanism for the conventional enamel used was not fully understood, but it was expected to be more complicated that the mechanism proposed above, owing to the presence of two interfaces in its structure.

Results of surface potential decay measurements allowed for deriving the trap density distribution and the charge carrier mobility of the insulations. The addition of chromium oxide gave rise to the shallow traps, probably appearing in the interfacial regions between the fillers and the polymer. The charge carrier mobility was ~$10^{-16}$ $m^2V^{-1}s^{-1}$ for both hole and electron for the consider materials and a weak field-dependent behavior was observed.

## 5.3 Partial discharge measurements

Measurements of PD characteristics have been carried out for the conventional and $Cr_2O_3$-filled enamels exposed to PWM voltage with different rise times. The filled enamel was characterized by lower levels of both PD inception and extinction, which might be related to the enhancement of electric field at wire surfaces due to the presence of the highly dispersive filler. The PD exposure was reduced for the filled enamel, but only at the shortest voltage rise time, while the effect was not observed at longer rise times. This property could be due to the decay of charges on wire surface. As it was found by surface potential measurements in chapter 2, charges could remain on the conventional enamel surface for longer time duration, thus, they might enhance the electric field in the air gap between the wires after polarity reversal. As a result, the field strength could be reduced that led to the improved PD performance of the filled enamel. The PD performance of both the enamels at filtered voltages requires further investigations.

In addition, the preliminary results showed the substantial decrease of PD amplitude with increasing voltage rise time. This indicated the significance of using filters for reducing the applied voltage steepness in order to lengthen insulation life time. This measure should be considered in compromise with the use of new PD-resistance enamel insulations.

# 6 Future work

Suggestions for future work include the developments of mathematical description and computer simulation for the surface potential decay process of the enamel insulations with multilayered structure. The transport equations introduced in [37] should be extended to consider the effect of the interface in the particular enamels used, and based on this, a computer model can be developed taking into account the contributions of charge injection, dipolar polarization, and intrinsic conduction in the potential decay process. The simulated results are to be compared with the experimental data for model validation. The hypotheses of the decay process proposed in the present study need to be proved by the developed model.

Continuation of the PD measurements for the enameled wires is necessary. From the statistical point of view, the use of experimental data collected from an increased number of voltage cycles would provide a better representation for the PD performance of the materials. In relation to this, the erosion patterns on wire surfaces would be interesting to monitor by using a microscope. Several carrier frequencies of PWM waveforms and more filtering levels should be applied. The obtained trap density distribution and the interaction of charges with the insulations revealed by the computer simulation might be useful in interpreting the measured PD characteristics.

# References


[1] D. Fabiani and G. C. Montanari, "The effect of voltage distortion on ageing acceleration of insulation systems under partial discharge activity," *IEEE Electrical Insulation Magazine,* vol. 17, pp. 24-33, 2001.

[2] D. Fabiani, G. C. Montanari, A. Cavallini, and G. Mazzanti, "Relation between space charge accumulation and partial discharge activity in enameled wires under PWM-like voltage waveforms," *IEEE Transactions on Dielectrics and Electrical Insulation,* vol. 11, pp. 393-405, 2004.

[3] S. U. Haq, S. H. Jayaram, and E. A. Cherney, "Evaluation of medium voltage enameled wire exposed to fast repetitive voltage pulses," *IEEE Transactions on Dielectrics and Electrical Insulation,* vol. 14, pp. 194-203, 2007.

[4] S. U. Haq, S. H. Jayaram, and E. A. Cherney, "Performance of nanofillers in medium voltage magnet wire insulation under high frequency applications," *IEEE Transactions on Dielectrics and Electrical Insulation,* vol. 14, pp. 417-426, 2007.

[5] T. Ozaki, T. Imai, F. Sawa, T. Shimizu, and F. Kanemitsu, "Partial discharge resistant enameled wire," in *Proceedings of International Symposium on Electrical Insulating Materials* 2005, pp. 184-187.

[6] A. Bjorklund, H. Siberg, and P. Paloniemi, "Accelerated ageing of a partial discharge resistant enameled round wire [motor winding]," in *Proceedings of Electrical Electronics Insulation and Electrical Manufacturing & Coil Winding Conference*, 1995, pp. 417-419.

[7] G. Paulsson, F. Sahlen, H. Hillborg, A. Björklund, M. Takala, and J. Andersson, "New type of PD-resistant enameled wire," in *12th International Electrical Insulation Conference* Birmingham, UK, 2013, pp. 169-174.

[8] S. Diaham and M.-L. Locatelli, "Dielectric properties of polyamide-imide," *J. Phys. D: Appl. Phys.*, vol. 46, p. 185302, 2013.

[9] S. K. Dolui, D. Pal, and S. Maiti, "Synthesis of a Novel Polyesterimide," *J. Appl. Polym. Sci.*, vol. 30, pp. 3867-3878, 1985.

[10] J. A. Crawford and R. W. Vest, "Electrical Conductivity of Single Crystal Cr2O3," *Journal of Applied Physics,* vol. 35, pp. 2413-2418, 1964.

[11] R. C. Ku and W. L. Winterbottom, "Electrical conductivity in sputter-deposited chromium oxide coatings," *Thin Solid Films,* vol. 127, pp. 241-256, 1985.

[12] P. R. Chapman, R. H. Griffith, and J. D. F. Marsh, "The Physical Properties of Chromium Oxide-Aluminium Oxide Catalysts. II. Electrical Properties," *Proceeding of the Royal Society, Series A, Mathematical, Physical Sciences,* vol. 224, pp. 419-426, 1954.

[13] A. Holt and P. Kofstad, "Electrical conductivity and defect structure of Cr2O3. II. Reduced temperatures (<1000°C)," *Solid State Ionics,* vol. 69, pp. 137-143, 1994.

[14] P. H. Fang and W. S. Brower, "Dielectric Constant of Cr2O3 Crystals," *Physical Review,* vol. 129, pp. 1561-1561, 1963.

[15] IEC Standard 60093, "Methods of Test for Volume Resistivity and Surface Resistivity of Solid Electrical Insulating Materials," 1980.

[16] X. Xu, "Enhancements in dielectric response characterization of insulation materials," Licenciate thesis, Chalmers University of Technology, 2013.

[17] X. Ma, N. H. Lee, H. J. Oh, J. S. Hwang, and S. J. Kim, "Preparation and characterization of silica/polyamide-imide nanocomposite thin films," *Nanoscale Res. Lett.*, vol. 5, pp. 1846-1851, 2010.

[18] M. Hasegawa, Y. Sakamoto, Y. Tanaka, and Y. Kobayashi, "Poly(ester imide)s possessing low coefficients of thermal expansion (CTE) and low water absorption (III). Use of bis(4-aminophenyl)terephthalate and effect of substituents," *European Polymer Journal,* vol. 46, pp. 1510-1524, 2010.

[19] T. A. Hahn, "Thermal expansion of copper from 20 to 800 K—Standard reference material 736," *Journal of Applied Physics,* vol. 41, pp. 5096-5101, 1970.

[20] A. K. Jonscher, *Dielectric Relaxation in Solids*. London: Chelsea Dielectrics Press, 1983.

[21] H. Scher and R. Zallen, "Critical density in percolation processes," *J. Chem. Phys.,* vol. 53, pp. 3759-3761, 1970.

[22] R. M. Hill and L. A. Dissado, "The temperature dependence of relaxation processes," *J. Phys. C: Solid State Phys,* vol. 15, pp. 5171-5193, 1982.

[23] E. Tuncer and S. M. Gubanski, "Electrical properties of filled silicon rubber," *J. Phys.: Condens. Matter,* vol. 12, pp. 1873-1897, 2000.

[24] Y. V. Serdyuk, A. D. Podoltsev, and S. M. Gubanski, "Numerical simulations of dielectric properties of composite material with periodic structure," *J. Electrostatics,* vol. 63, pp. 1073-1091, 2005.

[25] O. Wiener, "Die Theorie des mischkörpers fur das Feld der Stationären Strömung," *Abh. Math. Phys. Kl. Akad. Wiss. Leipzig,* vol. 32, pp. 509-604, 1912.

[26] T. Tanaka, M. Kozako, N. Fuse, and Y. Ohki, "Proposal of a multi-core model for polymer nanocomposite dielectrics," *IEEE Transactions on Dielectrics and Electrical Insulation,* vol. 12, pp. 669-681, 2005.

[27] T. Okamoto, K. Abe, Y. Itoh, and T. Umemura, "Partial discharge resistant mechanism of newly developed enameled wire," in *Annual Report., Conference on Electrical Insulation and Dielectric Phenomena,* 1997, pp. 512-515.

[28] P. Molinie, "Measuring and modeling transient insulator response to charging: the contribution of surface potential studies," *IEEE Transactions on Dielectrics and Electrical Insulation,* vol. 12, pp. 939-950, 2005.

[29] S. Kumara, "Electrical charges on polymeric insulator surfaces and their impact on flashover performance," PhD dissertation, Chalmers University of Technology, Gothenburg, Sweden, 2012.

[30] J. G. Simmons and M. C. Tam, "Theory of Isothermal Currents and the Direct Determination of Trap Parameters in Semiconductors and Insulators Containing Arbitrary Trap Distributions," *Physical Review B,* vol. 7, pp. 3706-3713, 1973.

[31] P. K. Watson, "The transport and trapping of electrons in polymers," *IEEE Transactions on Dielectrics and Electrical Insulation,* vol. 2, pp. 915-924, 1995.

[32] P. K. Watson, "The energy distribution of localized states in polystyrene, based on isothermal discharge measurements," *J. Phys. D: Appl. Phys.,* vol. 23, pp. 1479-1484, 1990.

[33] P. Llovera and P. Molinie, "New methodology for surface potential decay measurements: application to study charge injection dynamics on polypropylene films," *IEEE Transactions on Dielectrics and Electrical Insulation,* vol. 11, pp. 1049-1056, 2004.

[34] H. J. Wintle, "Surface Charge Decay in Insulators with Nonconstant Mobility and with Deep Trapping," *Journal of Applied Physics,* vol. 43, pp. 2927-2930, 1972.

[35] T. J. Sonnonstine and M. M. Perlman, "Surface-potential decay in insulators with field-dependent mobility and injection efficiency," *Journal of Applied Physics,* vol. 46, pp. 3975-3981, 1975.

[36] M. M. Perlman, T. J. Sonnonstine, and J. A. St.Pierre, "Drift mobility determinations using surface potential decay in insulators," *Journal of Applied Physics,* vol. 47, pp. 5016-5021, 1976.

[37] H. von Berlepsch, "Interpretation of surface potential kinetics in HDPE by a trapping model," *J. Phys. D: Appl. Phys.,* vol. 18, pp. 1155-1170, 1985.

[38] V. I. Arkhipov, J. A. Popova, and A. I. Rudenko, "Space-charge perturbed dispersive transport in disordered dielectrics," *J. Electrostatics,* vol. 18, pp. 23-37, 1986.

[39] W. Tomaszewicz, "Surface-potential decay of disordered solids," *J. Electrostatics,* vol. 51, pp. 340-344, 2001.

[40] M. Ieda, G. Sawa, and U. Shinohara, "A decay process of surface electric charges across polyethylene film," *Japan. J. Appl. Phys.,* vol. 6, pp. 793-794, 1967.

[41] S. Sahlia, A. Bellela, Z. Ziaria, A. Kahlouchea, and Y. Seguib, "Measure and analysis of potential decay in polypropylene films after negative corona charge deposition," *J. Electrostatics,* vol. 57, pp. 169-181, 2003.

[42] H. J. Wintle, "Decay of Static Electrification by Conduction Processes in Polyethylene," *Journal of Applied Physics,* vol. 41, pp. 4004-4007, 1970.

[43] S. Kumara, Y. V. Serdyuk, and S. M. Gubanski, "Surface charge decay on polymeric materials under different neutralization modes in air," *IEEE Transactions on Dielectrics and Electrical Insulation,* vol. 18, pp. 1779-1788, 2011.

[44] H. Sjostedt, S. M. Gubanski, and Y. V. Serdyuk, "Charging Characteristics of EPDM and Silicone Rubbers Deduced from Surface Potential Measurements," *IEEE Transactions on Dielectrics and Electrical Insulation,* vol. 16, pp. 696-703, 2009.

[45] A. R. Frederickson and J. R. Dennison, "Measurement of conductivity and charge storage in insulators related to spacecraft charging," *IEEE Transactions on Nuclear Science,* vol. 50, pp. 2284-2291, 2003.

[46] N. W. Green, A. R. Frederickson, and J. R. Dennison, "Experimentally Derived Resistivity for Dielectric Samples From the CRRES Internal Discharge Monitor," *IEEE Transactions on Plasma Science,* vol. 34, pp. 1973-1978, 2006.

[47] P. Molinie, M. Goldman, and J. Gatellet, "Surface potential decay on corona-charged epoxy samples due to polarization processes," *J. Phys. D: Appl. Phys.,* vol. 28, pp. 1601-1610, 1995.

[48] P. Molinie, "Potential decay interpretation on insulating films: necessity of combining charge injection and slow volume polarization processes," in *Proc. 7th Int. Conf. Dielectr. Mat. Meas. Appl.,* 1996, pp. 50-55.

[49] D. C. Faircloth and N. L. Allen, "High resolution measurements of surface charge densities on insulator surfaces," *IEEE Transactions on Dielectrics and Electrical Insulation,* vol. 10, pp. 285-290, 2003.

[50] S. Kumara, I. R. Hoque, S. Alam, Y. V. Serdyuk, and S. M. Gubanski, "Surface charges on cylindrical polymeric insulators," *IEEE Transactions on Dielectrics and Electrical Insulation,* vol. 19, pp. 1076-1083, 2012.

[51] E. Kuffel, W. S. Zaengl, and J. Kuffel, *High Voltage Engineering: Fundamentals*: Newnes, 2000.

[52] W. S. Zaengl, "Dielectric spectroscopy in time and frequency domain for HV power equipment. I. Theoretical considerations," *IEEE Electrical Insulation Magazine,* vol. 19, pp. 5-19, 2003.

[53] D. W. Vance, "Surface Charging of Insulators by Ion Irradiation," *Journal of Applied Physics,* vol. 42, pp. 5430-5443, 1971.

[54] Z. Xu, L. Zhang, and G. Chen, "Decay of electric charge on corona charged polyethylene," *J. Phys. D: Appl. Phys.,* vol. 40, pp. 7085–7089, 2007.

[55] G. Chen, "A new model for surface potential decay of corona-charged polymers," *J. Phys. D: Applied Physics,* vol. 43, p. 055405, 2010.

[56] T. Takada, "Acoustic and optical methods for measuring electric charge distributions in dielectrics," *IEEE Transactions on Dielectrics and Electrical Insulation,* vol. 6, pp. 519-547, 1999.

[57] W.-W. Shen, H.-B. Mu, G.-J. Zhang, J.-B. Deng, and D.-M. Tu, "Identification of electron and hole trap based on isothermal surface potential decay model," *Journal of Applied Physics,* vol. 113, pp. 083706-083706-6, 2013.

[58] M. Watanabe, K. Sanui, N. Ogata, T. Kobayashi, and Z. Ohtaki, "Ionic conductivity and mobility in network polymers from poly(propylene oxide) containing lithium perchlorate," *Journal of Applied Physics,* vol. 57, pp. 123-128, 1985.

[59] E. Persson, "Transient effects in application of PWM inverters to induction motors," *IEEE Transactions on Industry Applications,* vol. 28, pp. 1095-1101, 1992.

[60] J. C. G. Wheeler, "Effects of converter pulses on the electrical insulation in low and medium voltage motors," *IEEE Electrical Insulation Magazine,* vol. 21, pp. 22-29, 2005.

[61] P. Bidan, T. Lebey, G. Montseny, and J. Saint-Michel, "Transient voltage distribution in inverter fed motor windings: experimental study and modeling," *IEEE Transactions on Power Electronics,* vol. 16, pp. 92-100, 2001.

[62] A. Cavallini, D. Fabiani, and G. Montanari, "Power electronics and electrical insulation systems - Part 1: Phenomenology overview," *IEEE Electrical Insulation Magazine,* vol. 26, pp. 7-15, 2010.

[63] T. Bengtsson, F. Dijkhuizen, L. Ming, F. Sahlen, L. Liljestrand, D. Bormann, R. Papazyan, and M. Dahlgren, "Repetitive fast voltage stresses-causes and effects," *IEEE Electrical Insulation Magazine,* vol. 25, pp. 26-39, 2009.

[64] B. Sonerud, T. Bengtsson, J. Blennow, and S. M. Gubanski, "Dielectric heating in insulating materials subjected to voltage waveforms with high harmonic content," *IEEE Transactions on Dielectrics and Electrical Insulation,* vol. 16, pp. 926-933, 2009.

[65] E. Sharifi, S. H. Jayaram, and E. A. Cherney, "Analysis of thermal stresses in medium-voltage motor coils under repetitive fast pulse and high-frequency voltages," *IEEE Transactions on Dielectrics and Electrical Insulation,* vol. 17, pp. 1378-1384, 2010.

[66] M. Kaufhold, H. Aninger, M. Berth, J. Speck, and M. Eberhardt, "Electrical stress and failure mechanism of the winding insulation in PWM-inverter-fed low-voltage induction motors," *IEEE Transactions on Industrial Electronics,* vol. 47, pp. 396-402, 2000.

[67] F. Guastavino and A. Dardano, "Life tests on twisted pairs in presence of partial discharges: influence of the voltage waveform," *IEEE Transactions on Dielectrics and Electrical Insulation,* vol. 19, pp. 45-52, 2012.

[68] E. Lindell, T. Bengtsson, J. Blennow, and S. M. Gubanski, "Influence of rise time on partial discharge extinction voltage at semi-square voltage waveforms," *IEEE Transactions on Dielectrics and Electrical Insulation,* vol. 17, pp. 141-148, 2010.

[69] W. Yin, "Failure mechanism of winding insulations in inverter-fed motors," *IEEE Electrical Insulation Magazine,* vol. 13, pp. 18-23, 1997.

[70] L. Zhou and S. A. Boggs, "High frequency attenuating cable for protection of low-Voltage AC motors fed by PWM inverters," *IEEE Transactions on Power Delivery,* vol. 20, pp. 548-553, 2005.

[71] H. Kikuchi and H. Hanawa, "Inverter surge resistant enameled wire with nanocomposite insulating material," *IEEE Transactions on Dielectrics and Electrical Insulation,* vol. 19, pp. 99-106, 2012.

[72] IEC Standard 60851-5, "Winding wires - Test methods, Part 5: Electrical properties," 2008.

[73] T. Hammarstrom, T. Bengtsson, J. Blennow, and S. Gubanski, "PD properties when varying the smoothness of synthesized waveforms," *IEEE Transactions on Dielectrics and Electrical Insulation,* vol. 20, pp. 2035-2041, 2013.